2020

ELECTROSPUN NANOFIBER SCAFFOLDS AS A PLATFORM FOR BREAST CANCER RESEARCH

Carolynn Que
Michigan Technological University, caque@mtu.edu

ELECTROSPUN NANOFIBER SCAFFOLDS AS A PLATFORM FOR BREAST CANCER RESEARCH

By

Carolynn A. Que

A THESIS

Submitted in partial fulfillment of the requirements for the degree of

MASTER OF SCIENCE

In Biomedical Engineering

MICHIGAN TECHNOLOGICAL UNIVERSITY

2020

This thesis has been approved in partial fulfillment of the requirements for the Degree of MASTER OF SCIENCE in Biomedical Engineering.

Department of Biomedical Engineering

Thesis Advisor: *Dr. Smitha Rao*

Committee Member: *Dr. Jeremy Goldman*

Committee Member: *Dr. Marina Tanasova*

Department Chair: *Dr. Sean Kirkpatrick*

Table of Contents

List of figures

List of tables

Preface

This work was completed in part with the help of Samerender Nagam Hanumantharao whose responsibilities included statistical analysis of Cell Titer Blue data and aiding in cell culture experiments as well as fiber fabrication and Brennan Vogl who imaged several samples, both of whom were co-authors in a recently published IEEE journal “Engineered Three-Dimensional Scaffolds Modulating Fate of Breast Cancer Cells Using Stiffness and Morphology Related Cell Adhesion” of which I have permission to use data from. Emily Nelson conducted the degradation studies. Dr. Tanasova’s lab in the Chemistry department synthesized the ManCou-H probe.

Acknowledgements

I have several people who I would like to recognize and thank for their support in helping me complete this work:

I would first and foremost like to thank my advisor, Dr. Smitha Rao for allowing me to work in the Biomedical Micro Devices lab as an undergraduate researcher and supporting and encouraging me to continue my education as a master's student.

I would like to thank my friends and family, including fellow lab members for their motivation and support. Specifically, I would like to extend my gratitude to my mom, dad, brother and sister for all their love and encouragement.

My friend, colleague and co-author, Samerender Nagam Hanumantharao for training me, challenging me and offering honest but positive criticism.

Adren Rigdon, for keeping me well fed and mentally sane with an open ear to my complaints and intermittent ping pong distractions.

I would also like to thank the faculty and staff at Michigan Technological University including my committee for their advice and recommendations. I would also like to thank, Dr. Kathryn Perrine in the chemistry department, Mr. Paul Fraley from the materials science and engineering department, as well as Mr. Owen Mills and the ACMAL department for helping characterize fibers.

Abstract

Tumorigenesis is a complex process involving numerous cellular signaling cascades and environmental factors. Here, we report the fabrication of 3D scaffolds with different morphologies obtained by to study cancer cell proliferation and migration. Using an FDA approved, biocompatible and biodegradable polymer Polycaprolactone (PCL), we electrospun nanofiber scaffolds having mesh, aligned, and honeycomb morphologies. The role of the morphology and cellular preferences to nutrition in cell adhesion and proliferation was assessed using scaffolds obtained by electrospinning PCL with fluorescent fructose-like molecular probes. Cell viability, cell morphology, localized cellular growth as related to scaffold morphology and availability of the fructose-like molecular probes were investigated. The changes in biophysical properties of tumor microenvironment with change in morphology of the scaffolds were observed. In vitro tests for proliferation, alignment and migration of human dermal fibroblasts (HDFa), normal breast epithelial cells (184B5), adenocarcinoma (MCF-7), pre-malignant (MCF10AneoT) and triple-negative (MDA-MB-231 on the scaffolds on days 1, 2, and 3 were carried out. The morphology of the scaffolds was characterized using FE-SEM while surface characterization was done using FTIR. Mechanical properties of the scaffolds were investigated using a Dynamic Mechanical Analyzer (DMA). Cell proliferation was assessed using CellTiter-Blue® Viability Assay; migration and cell-scaffold interactions were investigated using phalloidin for F-Actin. Our data indicates that while topographical features affected cell adhesion and proliferation, cell lines that responded to the fructose-like probes tended to be more invasive. Furthermore, the preference to a specific scaffold was greatly altered by the presence of the probes with MDA-MB-231 showing least preference after 72 hours and pre-malignant MCF10AneoT showing highest preference. However, there was no significant difference in the cell numbers between scaffolds with probes and those without for the pre-malignant cells while this difference was noticeable in the control cell lines. Hence, a relation between cell preferences, scaffold morphology and nutritional sources may be sought by further exploring this approach.

1 Introduction

1.1 Statistics

The Surveillance, Epidemiology and End Results Program (SEER) estimates about 1.8 million people will be diagnosed with cancer in the United States in 2019 alone [1]. It is also predicted that nearly 50% of these people will be diagnosed with breast, lung and bronchus, prostate, or colorectal cancers and that these four cancers will be responsible for roughly 50% of all cancer deaths in 2019 [2]. An estimated 270,000 men and women will be diagnosed with breast cancer in 2019. Approximately 12.8 percent of women will be diagnosed with female breast cancer at some point during their lifetime making it the most common cancer diagnosis in the US. Fortunately, in its early stages breast cancer is fairly treatable, however in later stages, after metastasis to distant tissues, the survival rate is only 27.4% making it an important area of study [3]. The average cost of treatment is between $20.000 and $100,000 depending on the severity [4] and anywhere from 5 to 10 years of hormone therapy after chemotherapy, radiation or surgery, sometimes all three [5].

1.2 Defining Cancer

Cancer is defined as a disease which manifests due to mutations in one or more genes causing uncontrolled cell growth and leading to the formation of a tumorous mass [6, 7]. The progression, size and location of the tumor defines the stage of cancer. Stage 0 is typically thought of as cancer free but abnormal cells with the potential to become cancerous have been found. This is sometimes referred to as carcinoma *in situ* cells present in this stage are called premalignant. Stage I indicates cancer exists in only a small area, this is usually considered early stage and tumors present are called primary tumors. Larger cancer which has grown into nearby tissues or lymph nodes are classified as stage II or III. Once the cancer has spread to distant parts of the body it is considered to have metastasized and is referred to as advanced or stage IV resulting in the presence of metastatic cells such as adenocarcinomas [8].

1.3 Current Treatment

Depending on the stage, different treatment options are available for patients. The National Breast Cancer Foundation offers the following summary of treatment options for different stages of breast cancer: In the case of a primary tumor, surgery is usually suggested in order to remove the tumor with a lumpectomy, partial mastectomy, or radical mastectomy. If it’s deemed necessary, some oncologists may also prescribe localized radiation and hormone therapy to ensure all dangerous cells are eradicated. Treatment options vary widely for stage II and III

cancers consisting of mastectomy, localized radiation, hormone therapy, chemotherapy, or in the most successful cases a combination of two or more treatments. Stage IV indicates the cancer has spread to distant tissues such as the brain bones, liver and lungs this stage is considered incurable however it has been shown to respond to a number of treatment options which could extend a patient's life several years [9].

1.4 Biology of Cancer

Unfortunately, because every patient is different, there is no one size fits all treatment option and in too many cases time, money, and resources are spent in identifying treatment options and may have severe side effects and ultimately may not work. Investigations into the inner workings of this disease could offer additional information for combating it. Numerous studies have shown differential characteristics when comparing the tumor microenvironment to a healthy physiological microenvironment [10]. Most notably, the tumor microenvironment is more acidic exhibiting a pH of around 6.8 compared to the more basic physiological pH of 7.4 [11]. This has been theorized to be due to the hypoxic, or deoxygenated conditions within a tumor which leads to anaerobic metabolism resulting in increased levels of acetic acid. The tumor microenvironment is also stiffer than the surrounding tissues and cancer cells typically have less stiff cellular membrane.

1.5 Our Approach

Since anaerobic metabolism doesn't yield the same amount of ATP as the Kreb's cycle, cancer cells have adapted and shortened the process by taking up fructose in addition to glucose to obtain a sufficient amount of energy for growth, proliferation, and metastasis. Fructose is transported to the cells via facilitative transporters, specifically GLUT5 (SLC2A5). This transporter has not been reported to be as active in non-cancerous cells [12]. The Warburg effect determined this affinity to anaerobic metabolism is present even in oxygenated conditions [13] making exploitation of the GLUT5 pathway using fructose an area of interest.

To examine the behavior of cancer cells and identify better treatment options *in vitro* models of the tumor microenvironment have been used. These models provide a low-cost research platform for cancer therapies, drug screening and insight on the mechanisms of metastasis by studying the cells in within the tumor, its stroma, extracellular matrix (ECM) and surrounding signaling molecules.

Current *in vitro* models such as transwell-based assays monitor cancer cell migration in response to some stimuli or condition such as chemo attractants, drug treatments or gene manipulation [14, 15]. These models, although useful with regards to cancer cell migration and invasion, don't offer a dynamic environment

such as that of the tumor microenvironment as the conditions are limited to single cell migration, invasion and trans endothelial migration in two dimensions.

Spheroids on the other hand are cell aggregates grown in suspension which closely resemble the spherical nature of a tumor. This makes them more useful for drug screening, studying immune interactions, and studying tumor growth and proliferation when compared to 2D cell culture. Sometimes spheroids are grown embedded in matrix and allows for studies of invasion, matrix remodeling and angiogenesis. Spheroids embedded in a matrix recapitulate transport properties cell-cell and cell-matrix interactions between the cells and the tumor microenvironment [16-18]. Due to their shape larger spheroids sustain oxygen and nutrient gradients which bear result in the emergence of a necrotic core which bare similarities to poorly vascularized physiological tumors [19]. Proliferation gradients have also been demonstrated in spheroid models resulting in protein and gene expression profiles more closely resembling those of clinical and *in vivo* gene expression profiles when compared to 2D culture [20]. These models are more costly and time consuming when compared to transwell assays. Spheroids also pose challenges to maintain uniformity and in the case of suspended spheroids don't account for the biophysical cues from the ECM.

I hypothesize nanofiber scaffolds composed of FDA approved biodegradable, biocompatible polymers and designed to offer controllable biophysical cues would provide a more physiologically accurate *in vitro* tumor model than transwell assays or spheroids. I further hypothesize the biochemical cues present in the tumor microenvironment can be imitated by incorporating signaling molecules into the scaffolds. The incorporation of fluorescent fructose probes is expected to offer insight into the metabolism of several cell lines on PCL nanofiber scaffolds of different topographical morphologies, affecting topotaxis and durotaxis. We also hope to investigate potential behavior of integrated drugs into PCL scaffolds.

2 Materials and Methods

2.1 Fiber Fabrication

2.1.1 Solution Preparation

All polymer solutions dissolved in chloroform were properly labeled and stirred on a hotplate protected from light at 32°C and 640 RPM (Fisherbrand™ Isotemp™ Stirring Hotplate) to reduce oxidation due to light exposure and prevent production of phosgene.

2.1.1.1 Polycaprolactone

Polycaprolactone (PCL) is an FDA approved, biodegradable polyester which has gained a lot of attention for its controllable mechanical properties and slow degradation rates. Its physiochemical state, chemical and biological properties, degradability and mechanical strength can all be adjusted allowing it to be used under harsh mechanical, physical and chemical conditions without significant loss of its properties.

A solution consisting of 20% PCL (Mw = 70,000 GPC; Scientific Polymer Products, USA) was prepared in Chloroform HPLC Grade (Sigma Aldrich, USA). The solution was heated and mixed away from light at 32°C and 640 RPM (Fisherbrand™ Isotemp™ Stirring Hotplate) until homogeneous.

2.1.1.2 ManCou-H Synthesis

The affinity of breast cancer cells to fructose allowed for the investigation of their metabolic preferences using fluorescent fructose-like molecules as probes. The biomedical microdevices lab partnered with Dr. Tanasova's team in the chemistry department at Michigan Technological University to test the fructose-like molecular probe ManCou-H [21-24]. ManCou-H is composed of mannitol with a coumarin as a fluorescent tag with a hydrogen located in the C_4 position.

D-Glucosamine hydrochloride (4.0g, 18.6 mmol, 1.0eq) was dissolved in water (40 ml) and stirred at room temperature for 5 hours. The solution was then cooled down with an ice bath. Once cooled, sodium nitrite (3.2g, 46.5 mmol, 2.5eq) was added followed by portion wise addition of Amberlite 120 H^+ (acidic) resin (30 mL). The reaction was then left to stir overnight at 0-4° C. The acidic resin was then filtration off and the reaction mixture was neutralized with Amberlite IRA-400 basic resin. The solution was then filtered, and the filtrate was dried via lyophilization to remove water. The desired compound was obtained as a yellow sicky solid in 79% yield (2.4 g) and was further used without purification (figure 2.1).

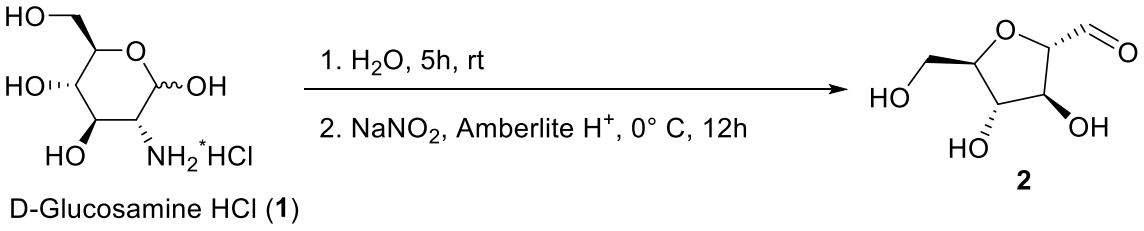

Figure 2.1 Synthesis of Mannitol using D-Glucosamine HCI the addition of water and sodium nitrate.

Aldehyde **2** (162.0 mg, 1.0 mmol, 1.0 eq) and 7-aminocoumarin (161.0mg, 1.0 mmol, 1.0 eq) were place into the round bottom flask and dissolved in MeOH/AcOH solution (10 ml, 95:5 v/v). The reaction mixture was allowed to stir at room temperature for 30 min. $NaBH_3CN$ (3.0 eq) was then added portion wise (3 x 1.0 mmol) every 30 min and the reaction was allowed to stir at room temperature overnight (8-10 h). The mixture was then concentrated to dryness under reduced pressure and subjected to column chromatography. The desired product was eluted using CH_2Cl_2: MeOH mixture (9:1 v/v). Samples for biological testing were further purified on a semi-preparative HPLC using a water-acetonitrile (5->30%) gradient (figure 2.2). The completed molecule with labeled sections is shown in figure 2.3.

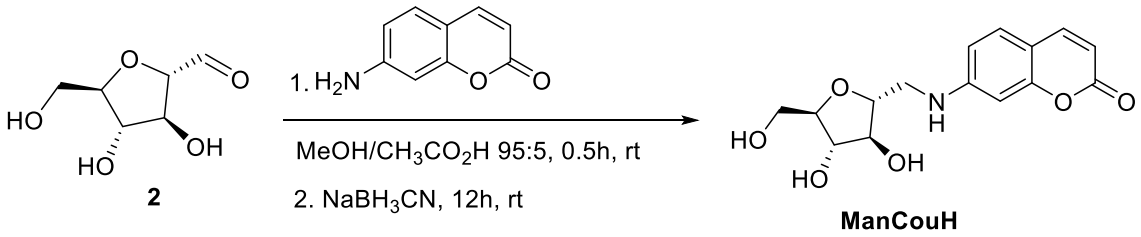

Figure 2.2 Synthesis of Mannitol to Coumarin in order to yield ManCou with a hydrogen in the functional C4 position.

Yellow solid, 169 mg, 55% yield. ^{1}H NMR (400 MHz, CD_3OD): δ, 7.76-7.36 (d, J = 9.2, 1H), 7.32-7.30 (d, J = 8.4, 1H), 6.68-6.65 (dd, J_1 = 2.4, J_2 = 8.4, 1H), 6.53 (d, J = 2.4, 1H), 6.01-5.99 (d, J = 9.2, 1H), 4.02-3.98 (m, 2H), 3.95-3.92 (m, 1H), 3.88-3.85 (m, 1H), 3.73-3.69 (dd, J_1 = 3.2, J_2 = 12.0, 1H), 3.66-3.61 (dd, J_1 = 5.6, J_2 = 12.0, 1H), 3.48-3.44 (dd, J_1 = 3.6, J_2 = 13.6, 1H), 3.38-3.32 (dd, J_1 = 6.8, J_2 = 13.6, 1H) ppm. ^{13}C NMR (100 MHz, CD_3OD): δ, 164.7, 158.1, 154.5, 146.5,

130.2, 112.3, 110.6, 109.1, 98.0, 85.3, 83.2, 80.3, 78.9, 63.3, 46.2 ppm. HRMS (ESI): *m/z* $[M + Na]^+$ calcd.

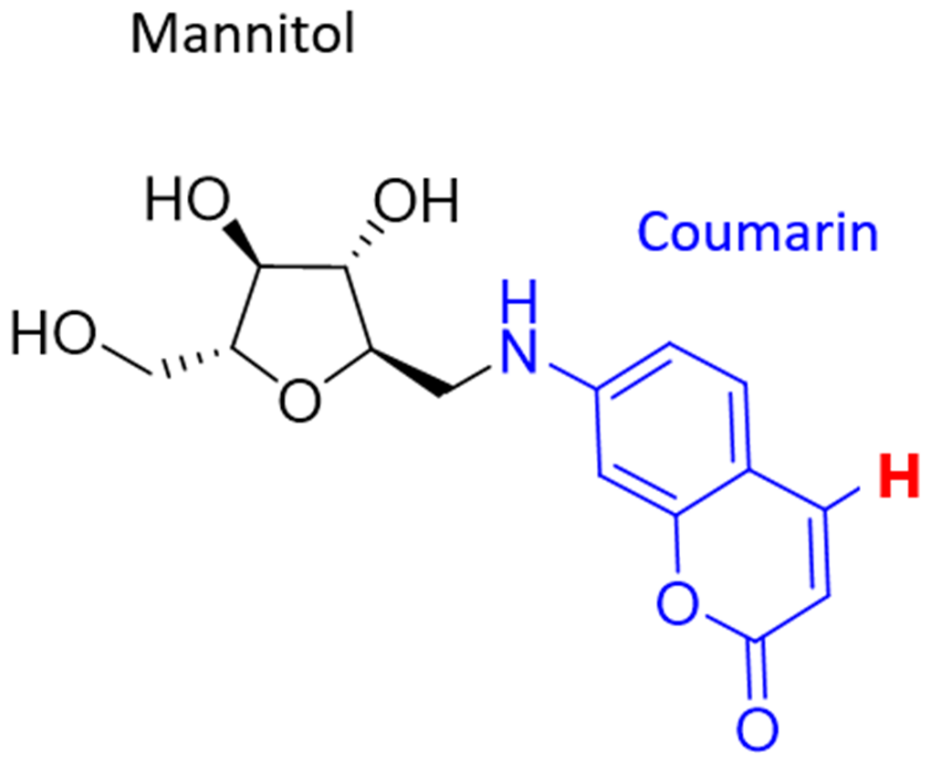

Figure 2.3 Complete ManCou-H molecule with coumarin fluorescent component shown in blue and GLUT5 binding Mannitol component in the black.

2.1.1.3 Polycaprolactone with ManCou-H

To produce biochemically different samples a 20% PCL solution similar to that described in 2.1.1.2 was mixed with a 20 µM final concentration of ManCou-H probe before being sonicated and degassed (Fisher Scientific™ CPXH Series Digital Ultrasonic Cleaners) for 30 min prior to electrospinning.

2.1.2 Electrospinning

Electrospinning exploits the electric field to draw charged threads of polymer solutions or polymer melts and continually produce fibers ranging from a few microns in diameter to ultrathin fibers in tens of nanometers. The electrospinning process is versatile, and flexible and has the potential to be scaled up for industrial production. This technique has been shown to have applications in tissue engineering for scaffold fabrication due to its ability to produce variable

fibrous scaffolds repeatedly, including topographies mimicking mesh, aligned and honeycomb structures similar to those of the natural ECM in the body.

The environmental factors like humidity and temperature, and tip-nozzle distance and as well as needle diameter were maintained at a constant throughout the electrospinning process (EM-DIG and EM-RTC; IME Technologies, Netherlands). These constants were 16% humidity, 70 °F, 17 cm and 0.6 mm, respectively. The parameters for all morphologies were held constant regardless of the presence of ManCou-H probe. For the fabrication of scaffolds with mesh morphologies, a voltage of 11 kV and rotational velocity of 150 RPM with polymer flow rate of 0.24 mL/hr was used whereas for scaffolds with aligned morphologies, a similar polymer flow rate and voltage was used with increased rotational speed of 275 RPM. The honeycomb structured scaffolds were fabricated by electrospinning at a rotational speed of 300 RPM with a feed rate of 0.18 mL/hr and applied voltage at the tip of the needle at 10 kV.

2.2 Fiber Characterization

2.2.1 Field Emission Scanning Electron Microscopy (FE-SEM)

Rather than using photons, Field Emission Scanning Electron Microscopy (FE-SEM) uses electrons liberated from a tungsten field emission source allowing for visualization of nanometer sized features. Once liberated, these electrons are accelerated in a high electrical field gradient which produces an ultralow vacuum environment. Electrons are then focused onto the samples of interest using electromagnetic lenses and apertures within the column to control the beam. Images are obtained by collecting electrons scattered by the object under interrogation on a fluorescent screen or cathode-ray tube (CRT). FE-SEM is capable of obtaining both backscatter and secondary electron images of conductive samples and can also be used for energy dispersive spectroscopy (EDS) for chemical microanalysis. Non-conductive samples must first be sputter coated with a thin layer of conductive metals most commonly carbon, gold, or platinum/palladium (Pt/Pd).

FE-SEM is a surface technique which allows for clear and accurate visualization of nanoscale features making it useful for polymer nanofiber visualization. To image the topographical morphology of the PCL fibers they were sputter coated with 5 nm of Pt/Pd. The fibers were then viewed while fixed to pin stub specimen mounts with carbon tape using an accelerating voltage of 10 kV. Various magnifications were used to obtain points of interest and the FESEM (Hitachi S-4700 FE-SEM). Greyscale images were captured and processed using ImageJ™ to measure the diameter of the nanofibers as well as their directionality using the ruler and Directionality™ plugin, respectively [25, 26].

2.2.2 Fourier Transform Infrared Spectroscopy (FTIR)

FTIR or Fourier Transform Infrared Spectroscopy is used to obtain an infrared spectrum of absorption or emission of a material in solid, liquid or gaseous state. When infrared light is radiated onto the polymer samples it is absorbed only when the energy is equal to one of the transitions among the discrete energy levels of the molecule.

The infrared spectroscopy of the scaffolds was characterized using Attenuated Fourier Transform Infrared Spectroscopy (Thermo Scientific™, Nicolet™ iS50 FTIR Spectrometer) from 4000–400 cm^{-1} at a resolution of 4 cm^{-1} with 256 scans.

2.2.3 Dynamic Mechanical Analysis (DMA)

Dynamic Mechanical Analysis (DMA) is an instrument which uses a specific destructive testing technique to measure the physical properties of solids and polymer melts. It then reports the modulus and damping, and can be programmed to measure force, stress, strain, frequency and temperature. To use a sample of known dimensions is loaded onto the clamp holder apparatus, a load is applied, and the strain is measured. Load displacement can be controlled either by applying sinusoidal stress and measuring the strain or the load can be increased gradually to the point of fracture.

The mechanical properties of each scaffold were measured by varying displacement with respect to time and obtaining stress until failure. The samples tested measured 0.75 cm in width, the length of each sample was measured by the DMA and the depth by a screw gauge. Each sample was then exposed to a stress and the strain was measured while the temperature was held constant at 37°C. Collected data was graphed and analyzed in Origin Pro™ (n=3).

2.2.4 Degradation

The slow degradation of PCL is a major contributing factor for its popularity in the field of biomaterials. The long degradation rate has led to PCL being used primarily in the replacement of hard tissues where healing takes longer. However, it can be extended to engineered soft tissues by decreasing its molecular weight and degradation time.

Scaffolds with and without ManCou-H probe of each morphology with side 1cm (n = 3) were cut and placed in Phosphate Buffer Solution (PBS) at 37°C. At time points 1, 2 and 3 hours the PBS was removed and saved at 4°C before being replaced by new PBS and placed back in the incubator. These samples were then run through a plate reader (Beckman Coulter DTX 880 Multimode Detector) at 360

nm excitation and 425 nm emission and concentration of probe leached was estimated.

2.3 Cell Seeding Experiments

2.3.1 Cell Culture

Adult human dermal fibroblasts (HDFa/ATCC® PCS-201-012™), adenocarcinoma (MCF7/ATCC® HTB-22™), triple negative malignant cells (MDA-MB-231 / ATCC® HTB-26™) and human breast epithelium (184B5 / ATCC® CRL-8799™) were purchased from America Type Cell Culture. The premalignant cancer cell line, MCF-10A-NeoT, was acquired from the Animal Model and Therapeutics Evaluation Core (AMTEC), Karmanos Cancer Institute, Wayne State University. Every cell line was maintained at 37°C, at 65% relative humidity, 5% CO_2. All cell lines except MCF-10A-NeoT and 184B5 was maintained in RPMI 1640 culture media supplemented with 10% fetal bovine serum (FBS) and 1% Penicillin Streptomycin (Pen Strep). MCF-10A-NeoT were cultured in DMEM F12 Ham (1:1) from Gibco with 1.05 mM $CaCl^2$, 10 mM HEPES, 10 µg/mL insulin, 20 ng/mL EGF, 0.5 µg/mL hydrocortisone, 5% horse serum, and 100 ng/mL cholera toxin. 184B5 was maintained in MEBM supplemented with MEGM Lonza/Clonetics Corporation kit (Kit Catalog No. CC-3150) minus the GA-1000 (gentamycin-amphotericin B mix).

2.3.2 Cell Seeding

Breast cell lines including, 184B5, MCF7, MCF-10A-NeoT, and MDA-MB-231 were seeded on scaffolds at a density of 1500 cells per scaffold of side 0.5 cm for cell viability experiments and scaffolds with dimensions 1.0 x 0.5 cm^2 for immunofluorescent imaging (n=3). The negative control, adult human dermal fibroblasts, HDFa were seeded at a concentration of 2500 cells per scaffold to account for the lower rate of proliferation (n=3). Cells were kept in their respective culture media on nanofiber scaffolds in non-treated tissue culture plates under standard cell culture conditions. As positive controls, 2500 HDFa cells per well and 1500 cells per well for each of the breast cancer cell lines under test were cultured on standard tissue culture treated plates.

2.4 Post-Cell Seeding Characterization

2.4.1 Immunostaining

Cells were fixed in 10 mL of 16% methanol-free formaldehyde solution diluted in 40 mL of PBS to produce a final concentration of 4% paraformaldehyde and visualized after 1, 2 and 3 days of growth via fluorescence microscopy. The

cells grown on ManCou-H integrated PCL fibers were stained with Alexa Fluor® 594 Phalloidin (Invitrogen, USA) under TX red filter, with and excitation and emission of 596 nm and 615 nm, respectively, as well as a DAPI filter, excitation and emission of 358 nm 461 nm, to illuminate the F-Actin within the cytoskeleton and the fluorescent fructose mimic, respectively. Cells grown on bare PCL fibers were also stained with Alexa Fluor® 594 Phalloidin (Invitrogen, USA) and imaged under the TX red filter but they were also stained with DAPI (4',6-diamidino-2-phenylindole) (Life Technologies, USA) for visualization of F-Actin and the A-T regions of the nucleus according to manufacturers' protocol.

2.4.2 Cell Alignment

Cell attachment and alignment along the fibers was quantified using image analysis software in MATLAB. The built in MATLAB functions for Otsu thresholding, and watershed were used to segment out the F-actin foreground of the immunostained images [27]. These segmented images were then run through another built in MATLAB function called 'regionprops' to be analyzed for their area and orientation [28, 29]. The standard deviation of the alignment orientation of each detected cell was then compared for each of the segmentation methods previously described. The average orientation deviation of these values was plotted using Microsoft Excel.

2.4.3 Cell Viability

The viability of the aforementioned cell lines on scaffolds with sides of approximately 0.5 cm (n=9) was obtained using CellTiter-Blue® Cell Viability Assay (Promega, Madison, WI). After 1, 2, and 3 days of growth in 48-wellplates (CellTreat scientific products®) the culture media was replaced and 20% volume of CellTiter-Blue® Cell Viability Assay reagent was added followed by 4 hours of incubation under standard culture conditions (37 °C, 65% RH and 5% CO_2). A 75µL aliquot of the incubated medium was transferred to a clear bottom 96-well opaque walled culture plate. Cell viability was determined using a plate reader (Beckman Coulter DTX 880 Multimode Detector) at 560 nm excitation and 590 nm emission.

2.4.4 Statistical Analysis

Statistical evaluation of the cell proliferation data was done using IBM® SPSS statistics V25 and OriginPro 2018b. Descriptive statistics was represented as mean ± standard error of mean (SEM) for cell viability and mean ± standard deviation (SD) for mechanical characterization of the scaffold. Fibers without ManCou-H probe were analyzed with one-way ANOVA followed by post-hoc Tukey's HSD test to calculate significance at $p<0.05$ between different days for each morphology of the scaffold. The same method was used to calculate the

significance between different cell lines for each morphology of the scaffold. The same method was used to analyze ManCou-H containing scaffolds.

3 Results

3.1 Fiber Characterization

By altering the electric field applied, the rotational velocity of the collecting mandrel, and the fluid flow rate during the electrospinning process three distinct topographical features were repeatably obtained using the same blend of polymeric materials. These three topographies are intended to imitate the natural ECM of various organs within the body. The applied electric field not only determines the initial elastic stress and bending instabilities in the jet [30], but it can also be used to control the spatial deposition of the fibers. This ability to control the spatial deposition is essential for creating topographical features [31]. The rotational velocity of the rotating mandrel collector helps better control the alignment, orientation and diameter of the fibers [32]. The applied electric field and rotational velocity work in conjunction as the applied average electric field determines the critical rotational velocity [33]. Typically, fibers exhibiting less alignment are produced using a lower rotational speed for the collector, alternatively, higher rotational speeds are used to fabricate scaffolds with fiber orientations perpendicular to the electric field vector. The flow rate at is typically a key parameter for controlling fiber diameter and distribution [34]. It initiates droplet shape, controls the trajectory of the jet, and maintains Taylor cone and deposition area [35, 36]. Higher flow rates result in higher fiber diameters and a higher deposition area whereas lower flow rates produce thinner fibers with a smaller deposition area.

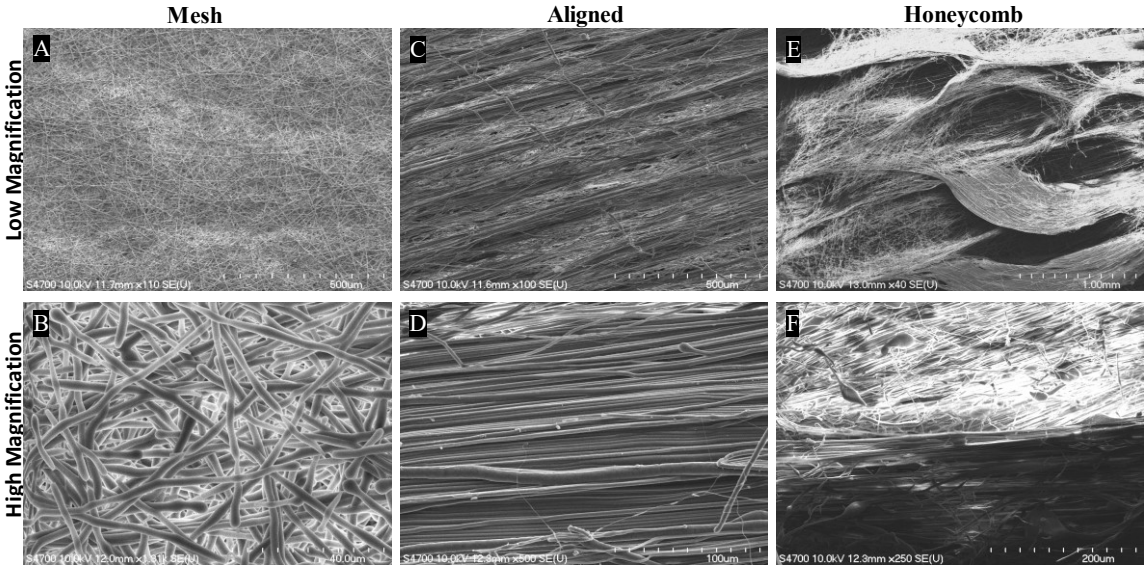

Figure 3.1 Field emission scanning electron microscopic (FESEM) images of the PCL scaffolds exhibiting different morphologies. The low magnification images (A, C, E) are present on the top while the high magnification images (B, D, F) are present in the bottom.

Visualization of the scaffolds was done using FE-SEM to analyze fiber morphology alignment, orientation, and diameter. Three distinct topographies with and without ManCou-H were initially visually classified as mesh, aligned, and honeycomb, shown in figure 4A, C and E, and figure 6A, C, and E, respectively. The lack of beading among all of the fiber scaffolds indicates an ideal concentration of PCL and chloroform solvent even in the case of fibers containing ManCou-H for electrospinning [37].

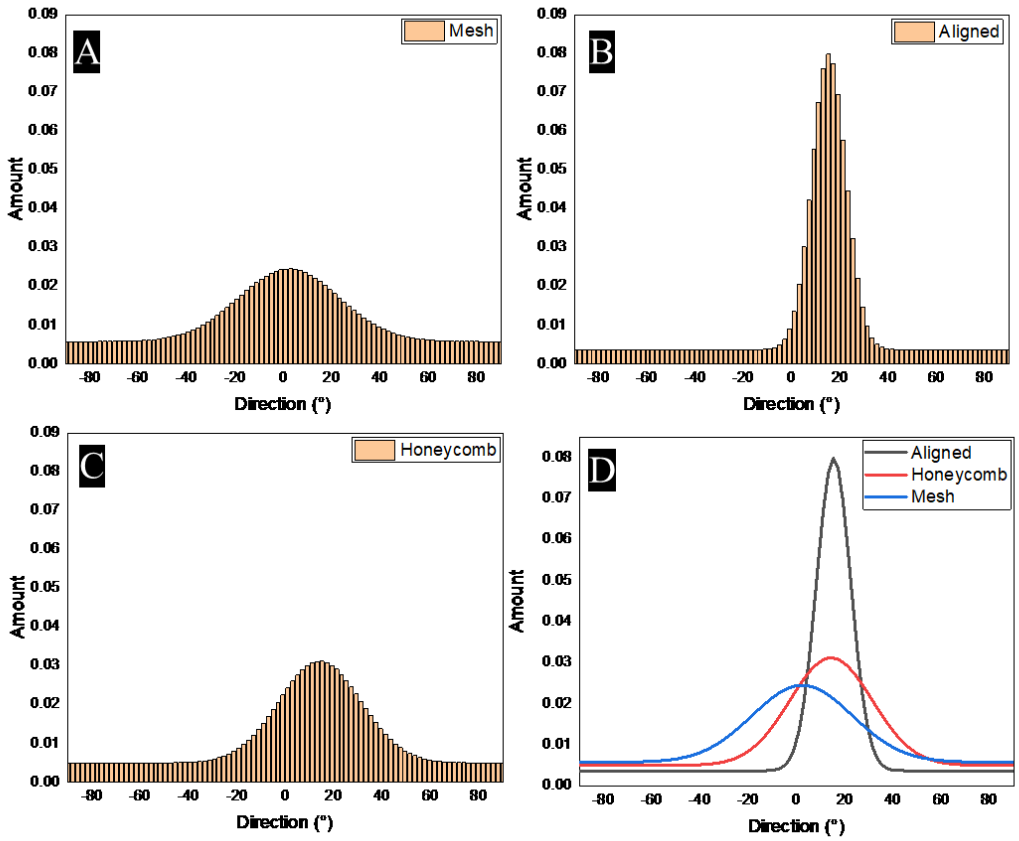

Figure 3.2 The deviation in alignment of the fibers in different morphologies of the bare scaffolds was characterized using the directionality plugin in ImageJ from the FESEM images used in figure 3.1 (n=5). The mesh fibers had a high dispersion of fibers in differ different angles. The aligned fibers had a high concentration of fibers in a narrow angle range with little amount of deviation in other directions. The honeycomb scaffolds had a broader range of deviation compared to the aligned scaffold but a much narrower distribution than the mesh scaffolds. A comparison between the three morphologies helps to compare the amount of alignment of the fibers and deviation from alignment.

The low magnification image of the mesh scaffolding without ManCou-H, (figure 3.1A) exhibited randomly oriented fibers which were densely packed forming a three-dimensional structure as seen by the cells. This dimensionality can

be seen from the change of contrast shown in the high magnification image shown in figure 3.1B which indicates the layers. A similar trend can be seen in the ManCou-H containing fibers shown in figures 3.3A and 3.3B, for low and high magnification respectively. Upon further analysis using the directionality plugin by ImageJ these scaffolds exhibited the highest amount of deviation as compared to the other samples (figure 3.2A and 3.4A). The fiber diameter was determined to be uniform among the mesh scaffold of 169.7 nm ± 10.7 nm.

Alternatively, the aligned scaffolds were found to have tightly packed fibers all oriented in the same direction. The deviation from alignment was calculated to be the lowest among the three morphologies (figure 3.2B and 3.4B). In the low magnification image (figure 3.3C) the fiber diameter appeared to show regions of larger and smaller diameter fibers in an alternating manner producing a channel like effect. The fiber diameter was determined to have a mean of 131.7 nm ± 21.77 nm A high magnification image (figure 3.3D) of the region containing fibers with larger diameters showed high concentrations of aligned fibers which overlapped one another to form a tight network.

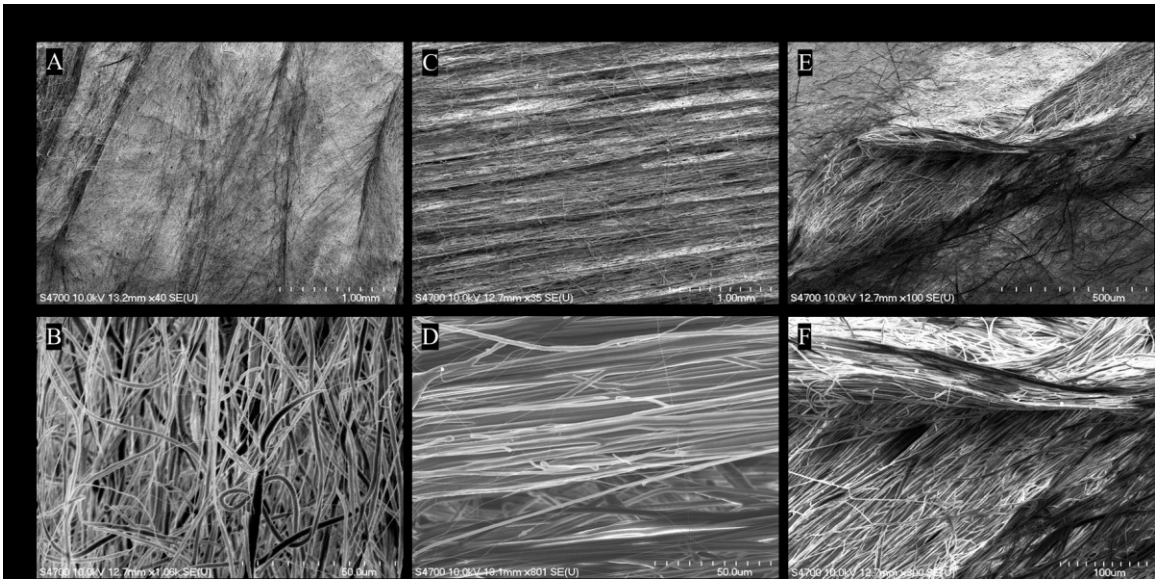

Figure 3.3 Field emission scanning electron microscopic (FESEM) images of the ManCou-H containing PCL scaffolds exhibiting different morphologies. The low magnification images (A, C, E) are present on the top while the high magnification images (B, D, F) are present in the bottom.

The low magnification image of the bare and ManCou-H containing honeycomb scaffolds, shown in figure 3.1E and 3.3E, respectively, shows the formation of interwoven fibers which interlocked in a specific repeating pattern to produce elongated, asymmetrical, honeycomb like structures. The arrangement of the honeycomb structure was characterized to have deep pores which exhibited a long-range order. Figure 3.1F and 3.3F, the low magnification image of the

honeycomb structure, shows the boundary of the pores, revealing densely packed aligned fibers present at the bottom of the pores and densely packed aligned fibers along the walls. The orientation of these aligned fibers at the wall and the floor of the pores was different, because of this, when analyzing the orientation there was a high deviation in alignment more closely related to the mesh morphology than the aligned despite the densely packed aligned fibers (figure 3.2C and 3C). The fiber diameter was calculated to have a mean of 144.1 µm ± 47.4 µm According to a series of experiments done by Bauer and colleagues, the formation of the dense network helps to mimic the biophysical conditions present during tumor-induced angiogenesis [38, 39].

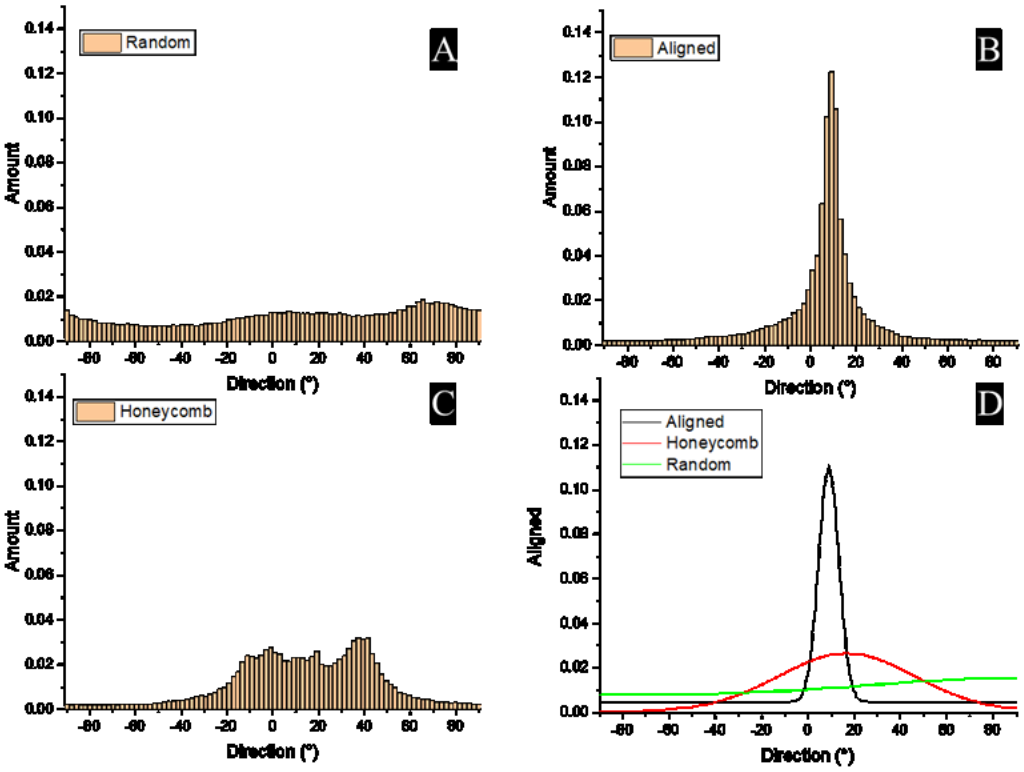

Figure 3.4 The deviation in alignment of the fibers in different morphologies of the scaffolds was characterized using the directionality plugin in ImageJ from the FESEM images used in figure 3.3 (n=5). The mesh fibers had a high dispersion of fibers in different angles. The aligned fibers had a high concentration of fibers in a narrow angle range with little amount of deviation in other directions. The honeycomb scaffolds had a broader range of deviation compared to the aligned scaffold but a much narrower distribution than the mesh scaffolds. A comparison between the three morphologies helps to compare the amount of alignment of the fibers and deviation from alignment.

3.2 Chemical Composition

Using ATR-FTIR spectroscopy, the surface characterization of the chemical bonds on the scaffolds in the absence and presence of ManCou-H was done shown in figure 3.1 and 3.3, respectively. The different morphologies inferred from FE-SEM and verified with image analysis using ImageJ showed similar absorbance intensities from the surface bonds which were extrapolated from infrared spectroscopy (figure 3.5A and 3.5B). This data cannot be used to draw a relationship between the isotropic nature of the fibers present in different scaffold morphologies because the incident beam was focused on a larger surface area rather than a single nanofiber. The peak seen at 1294 cm^{-1} is due to the stretching of C-O and C-C bonds in the crystalline phase [40]. As reported by Wang et. al the crystalline phase of PCL is accentuated during the electrospinning process[41]. This is due to the application of a high electric field causing the PCL chains to orient in a single direction [42]. The CH_2 vibration and O-C vibrations occur at 732 cm^{-1} and 961 cm^{-1} [43, 44], respectively while. bands seen at 1165 cm^{-1} and 1239 cm^{-1} correspond to asymmetric and symmetric stretching of the ester COO group [45]. The peak at 1365 cm^{-1} is associated with the CH_2 band vibrations [46]. The C=O vibration of ester corresponds to the peak present at 1723 cm^{-1} [47]. Asymmetric and symmetric stretching of the CH_2 group are the cause of the peaks present at 2865 cm^{-1} and 2942 cm^{-1} [48, 49]. Wavenumber where peaks exist according to the ATR-FTIR can be seen in table 3.1.

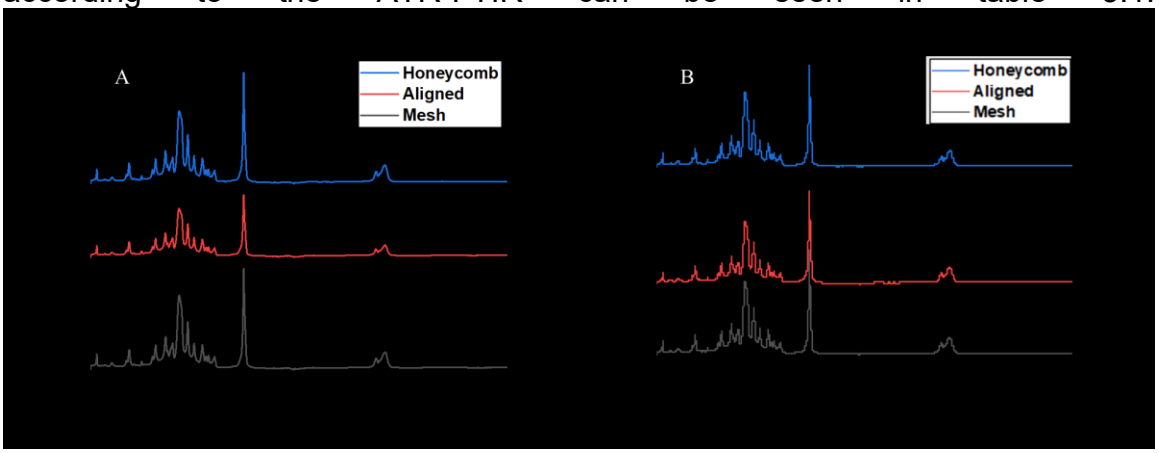

Figure 3.5 The surface and mechanical characterization of the PCL scaffolds of different morphologies was done. A) and B) Surface characterization was done using ATR-FTIR spectroscopy on bare and probe containing fibers, respectively. The peaks distinctive to the to the molecular bond orientations present in PCL were identified. All the morphologies had similar surface chemistry.

Table 3.1 Wavenumber where peaks exist according to ATR - FTIR

Wavenumber (cm^{-1})	**Significant Bonds**
2942 cm^{-1}	Asymmetric CH_2 stretching
2865 cm^{-1}	Symmetric CH_2 stretching
1723 cm^{-1}	C=O stretching of ester
1165 cm^{-1}	C—O stretching
732 cm^{-1}	CH_2 vibration
1239 cm^{-1}	Asymmetric C—O—C stretching
1365 cm^{-1}	CH_2 bending
961 cm^{-1}	O–C vibrations
1046 cm^{-1}	C—O—C stretching
1294 cm^{-1}	C–O and C–C stretching in the crystalline phase

3.3 Mechanical Characterization

Mechanical characterization of the scaffolds was done under isothermal conditions using DMA shown in figure 3.6. Each morphology demonstrated its own unique stress-strain behavior. The mechanical properties of the probe and non-probe containing scaffolds are summarized in table 3.2. The honeycomb scaffolds exhibited the highest average ultimate strength, Young's modulus, stiffness and strain at failure as compared to the other two morphologies. The Young's modulus and stiffness of the aligned scaffolds was comparable to the honeycomb

structures; however, the modulus of toughness is lower than that of the honeycomb scaffolds. As compared to the honeycomb and aligned scaffolds the mesh fiber morphology has relatively poor strength and toughness. The honeycomb and aligned scaffolds are ductile while the mesh scaffolds behave more plastically. The low rotational velocity of the collector and voltage applied during the fabrication process resulted in the mesh scaffolds elastomeric behavior [50]. Due to the fundamental truths of their morphology the aligned structures have better orientation in the microcrystalline regions which increases the Young's modulus of the scaffold [51, 52].

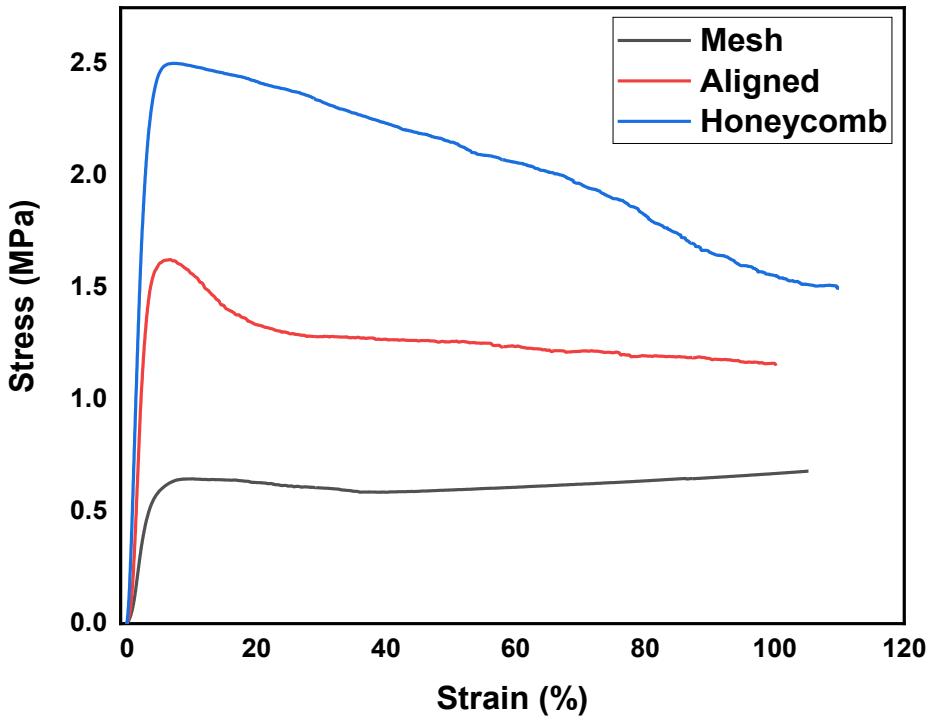

Figure 3.6 The mechanical properties of the scaffolds was characterized using DMA at isothermal conditions (37°C) and represented as stress-strain graph.

Table 3.2 Summary of the mechanical properties of the different morphologies of the scaffold.

	Mesh	Aligned	Honeycomb
Youngs Modulus (MPa)	0.155 ± 0.010	0.560 ± 0.118	0.569 ± 0.142
Modulus of Resilience	1.603 ± 0.643	2.945 ± 0.595	5.547 ± 0.045
Ultimate Tensile Strength (MPa)	0.818 ± 0.119	1.549 ± 0.073	2.341 ± 0.139
Strain at Failure (%)	104.512 ± 1.087	106.736 ± 5.990	107.512 ± 4.602
Modulus of Toughness	76.473 ± 10.636	136.885 ± 9.411	189.273 ± 28.404

3.4 Degradation

The release of the fluorescent probe was quantified at time points 24, 48 and 72 hours using a plate reader. These values were correlated to molarity of probe release on each day using a calibration curve (figure 3.7). A higher concentration of probe was shown to be released from the mesh scaffolds on day 1 followed by the mesh and lastly the honeycomb structures. Day 2 showed a higher release from the mesh scaffolds followed by the aligned then the honeycomb. Day 3 followed the same trend. This trend is expected as honeycomb and aligned fibers have a higher surface area resulting in a smaller proportion of ManCou-H within the scaffold and limiting the available probe to be released. The estimated amount of probe released for each sample type can be seen in table 3.3. Deviation in release could be the result of non-homogenous mixture of probe in PCL solution during the electrospinning process causing an uneven distribution of probe within the scaffold.

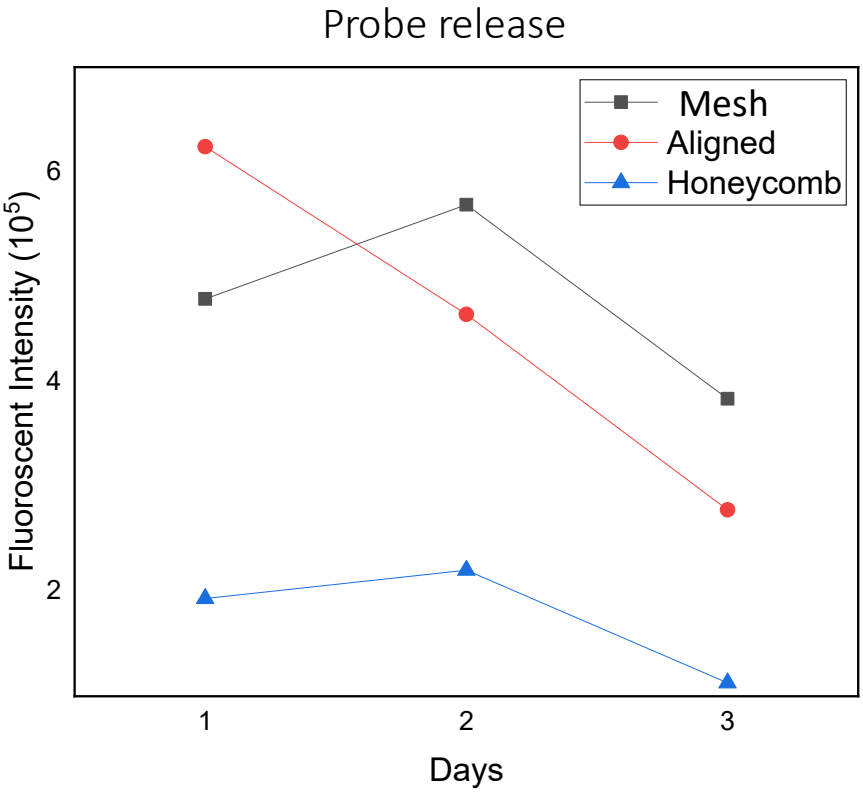

Figure 3.7 Observed drug released from PCL fibers in PBS using ManCou-H probe over a 3 day period for each fiber morphology the honeycomb values appear to exist below the deflection limit.

Table 3.3 Drug released from each fiber type measured in nanomolar

Day	Mesh	Aligned	Honeycomb
1	66.98811	110.5206	-18.7537
2	93.92716	62.55685	-10.6373
3	38.3986	6.639262	-42.8728

3.5 Immunofluorescent Imaging

Various stages of breast cancer progression were represented by using cell lines for healthy breast epithelium, adenocarcinoma, premalignant, and triple

negative / metastatic to evaluate the topotactic behavior of breast cancer cells. Cells grown on nanofiber scaffolds were stained and fixed 1, 2, and 3 days after seeding. Cells grown on bare PCL scaffolds were stained for actin in red and nucleus in blue, however the ManCou-H containing scaffolds were only stained for actin in red and any blue is due to the ManCou-H probe. Prior to seeding and staining the scaffolds were tested for to determine whether or not they bound the stain. It was found that the scaffolds do not express any background absorption of primary or secondary antibodies indicating the fluorescence seen in the images are cells. Had Alexa Fluor phalloidin 488 been used for actin staining NucRed™ could have been used to visualize the nucleus while still having the ability to differentiate the ManCou-H probe.

To get a better idea of how each cell line spans the 1.0x0.5 cm^2 scaffolds panoramas of the select cells on select scaffolds can be seen in figures 3.8 - 3.12. The adult human dermal fibroblasts can be seen in figure 3.8 on bare PCL scaffolds with a honeycomb morphology. Figure 3.9 shows the healthy breast epithelium on bare PCL scaffolds with a mesh morphology. Figure 3.10 shows MCF10ANeoT on aligned bare PCL scaffolds. Figure 3.11 shows MCF7 on bare honeycomb structured PCL scaffolds. Lastly the triple negative adenocarcinoma can be seen in figure 3.12 on aligned PCL fibers with the ManCou-H probe integrated into it. Qualitative classification for cell elongation, clumping, alignment to the scaffolds and infiltration within the scaffold are shown in figure 3.9. Phase images of fibers can be seen in Appendix A. In the future quantitative assessments of infiltration will be done using cryosectioning. This was attempted but a protocol for the cryosectioning of nanofibers is yet to be optimized.

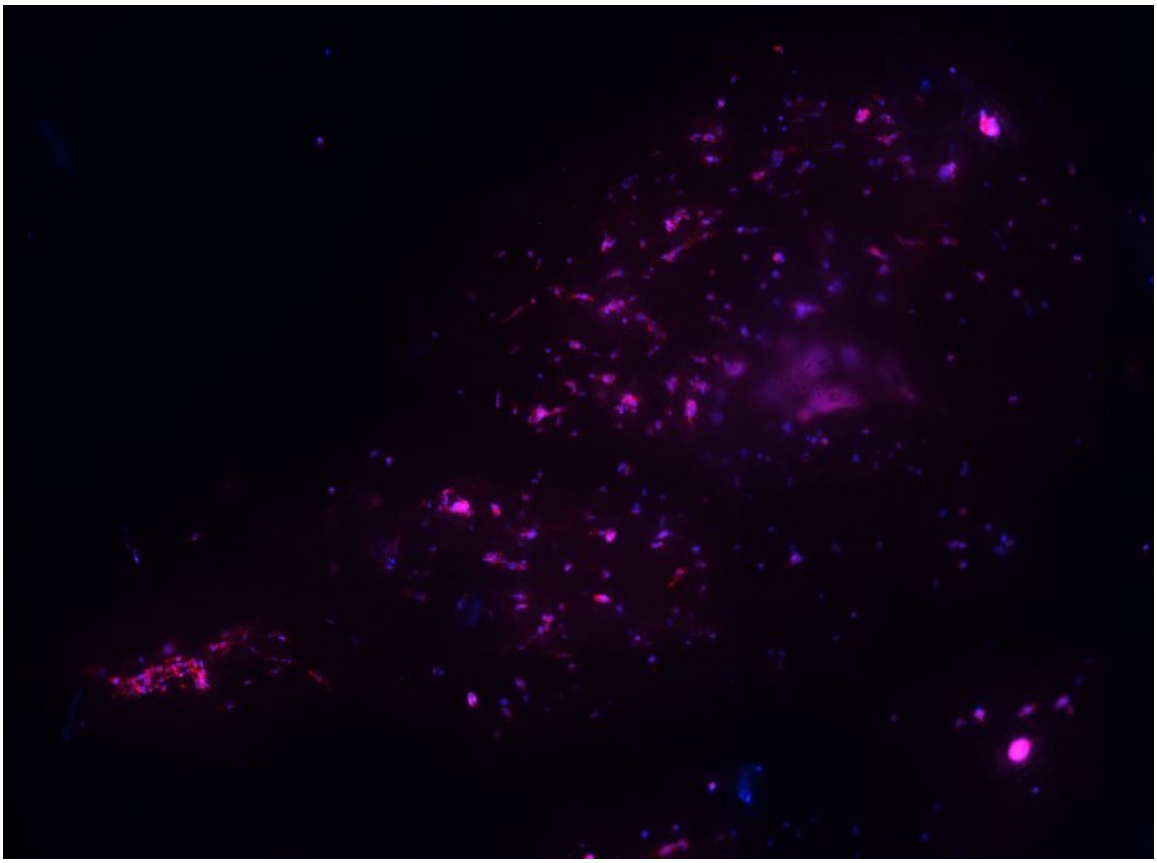

Figure 3.8 A panorama of adult human dermal fibroblasts on bare PCL scaffolds with a honeycomb morphology. The nuclei were stained with DAPI shown in blue and the F-actin filaments were stained with Alexa Fluor® 594 Phalloidin. The overlapping of the blue and red and dispersion by the fibers causes some of the cells to be seem pink in color. Images captured at 10X magnification.

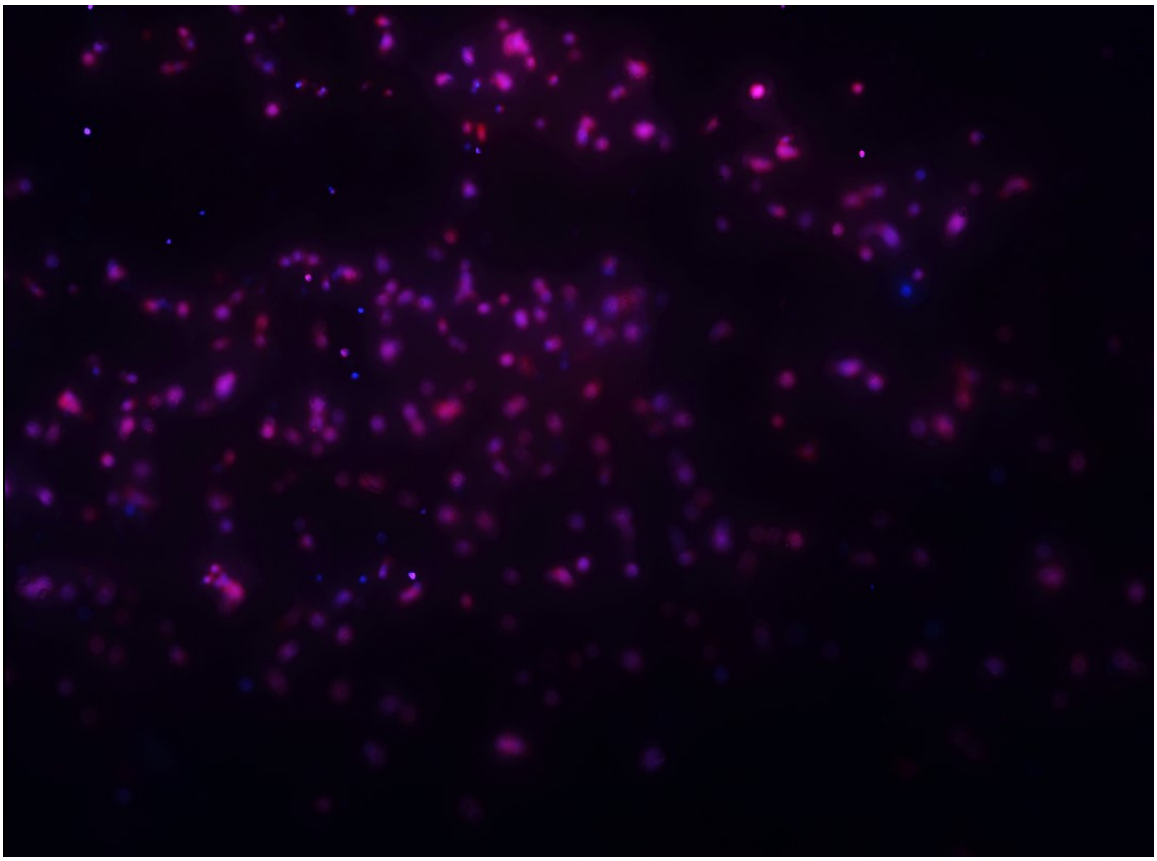

Figure 3.9 A panorama of the healthy breast epithelial cell line, 184B5, on bare PCL fibers with a mesh morphology. The nuclei were stained with DAPI shown in blue and the F-actin filaments were stained with Alexa Fluor® 594 Phalloidin. The overlapping of the blue and red and dispersion by the fibers causes some of the cells to be seem pink in color. Images captured at 10X magnification.

Figure 3.10 A panorama of premalignant cell line, MCF10ANeoT, on bare PCL scaffold with aligned morphology. The nuclei were stained with DAPI shown in blue and the F-actin filaments were stained with Alexa Fluor® 594 Phalloidin. The overlapping of the blue and red and dispersion by the fibers causes some of the cells to be seem pink in color. Images captured at 10X magnification.

Figure 3.11 A panorama of the ductal adenocarcinoma cell line, MCF7, on bare PCL scaffold with honeycomb morphology. The nuclei were stained with DAPI shown in blue and the F-actin filaments were stained with Alexa Fluor® 594 Phalloidin. The overlapping of the blue and red and dispersion by the fibers causes some of the cells to be seem pink in color. Images captured at 10X magnification.

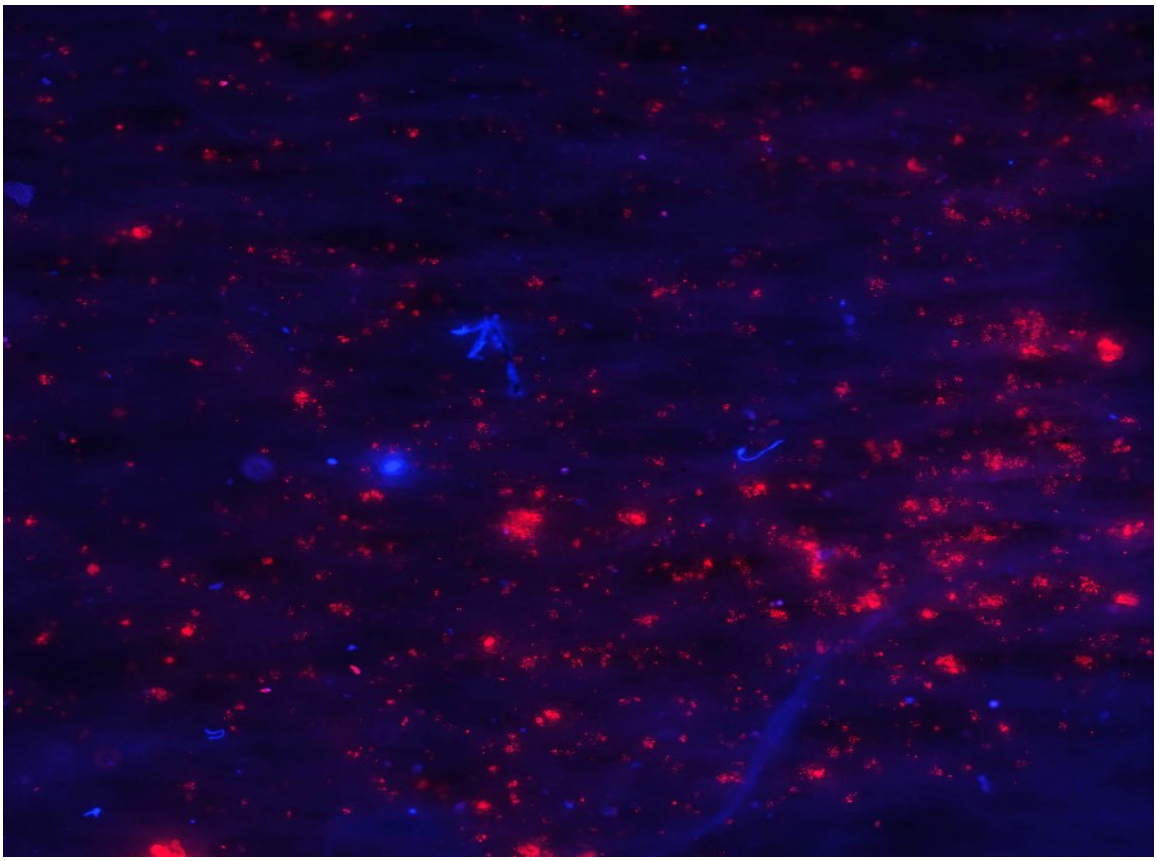

Figure 3.12 A panorama of the triple negative adenocarcinoma cell line, MDA-MB-231 on ManCou-H containing PCL fibers with an aligned morphology. The F-actin filaments were stained with Alexa Fluor® 594 Phalloidin shown in red, the ManCou-H probe is shown in blue. The overlapping of the blue and red and dispersion by the fibers causes some of the cells to be seem pink in color. Images captured at 10X magnification.

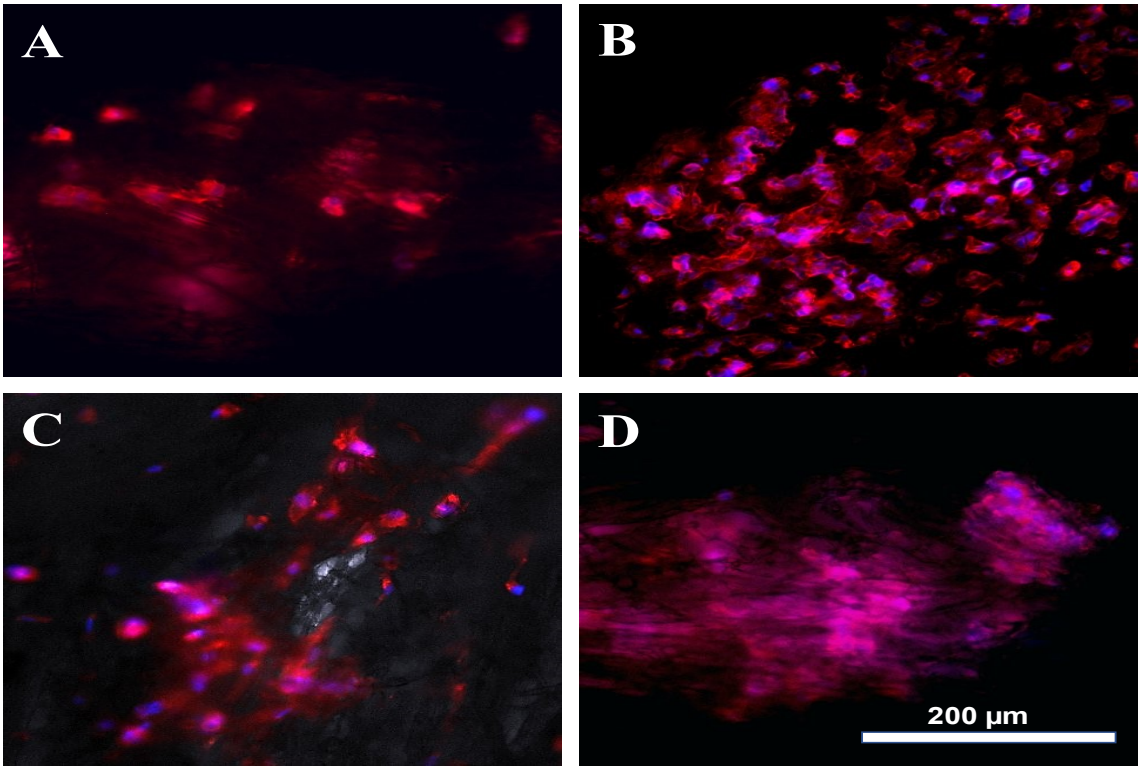

Figure 3.13 Phenotypes of the cells on scaffolds used to define cell behavior on the different morphologies of the scaffold. The phase images show the fibers and the overlaid fluorescent images show the alignment of nucleus against the orientation of the fibers. A) Aligned and elongated cells infiltrating into the scaffold. B) Clumped cells on scaffolds C) Cells aligning along the alignment of the scaffold D) The cells infiltrating through the different layers of the scaffolds in clumps.

3.5.1 HDFa

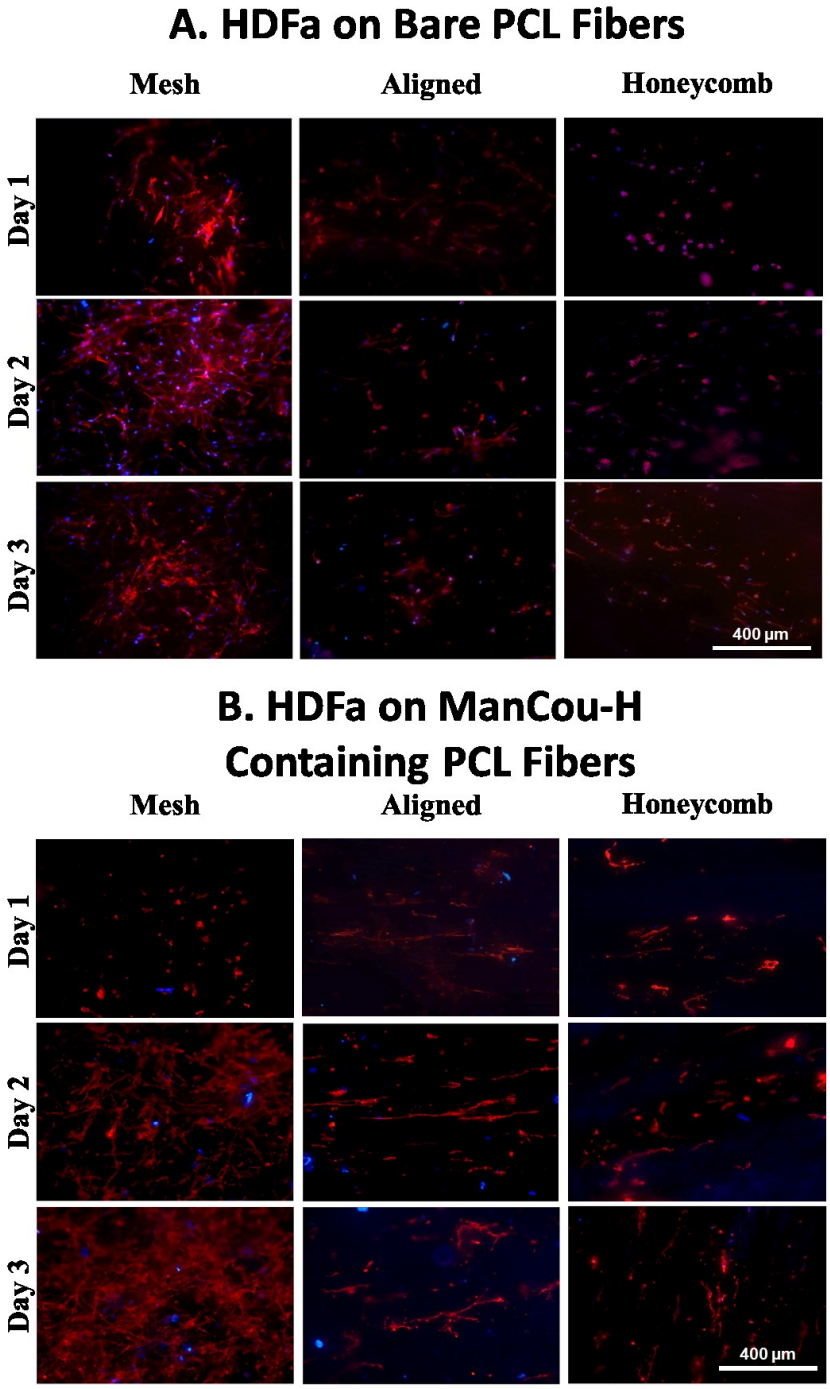

Figure 3.14 Fluorescent microscope images of Human Dermal Fibroblasts (HDFa) on different morphologies of B) PCL scaffold with and A) without ManCou-H probe on days 1, 2 and 3. A) the nuclei were stained with DAPI (blue) B) the probe is in blue and the F-actin filaments were stained with Alexa Fluor® 594 Phalloidin (red). The overlapping of

the blue and red and dispersion by the fibers causes some of the cells to be seem pink in color. Images captured at 10X magnification.

3.5.1.1 HDFa on Bare Scaffolds

The adult human dermal fibroblasts shown in figure 3.14A, maintained an elongated morphology despite the scaffold topography.

On non-probe containing fiber scaffolds the HDFa's had little to no cellular orientation on any morphology on any day. The mesh fiber scaffolds had cell clumping in specific regions on all days and scaffold infiltration increased from day 1 to day 3. On the aligned scaffolds the cells showed much less clumping on all days compared to the mesh although they had substantially infiltrated the scaffold on day 1 and continued to grow within the fibers through days 2 and 3. Cells on the honeycomb structure showed almost no clumping on day 1 but rather appeared to be spread out across the scaffold with some infiltration and some cellular orientation. By day 2 the cells began clumping in the porous regions of the scaffold with even more infiltration. Definitive cellular orientation is visible on day 3 as well as significant infiltration into the scaffold.

3.5.1.2 HDFa on ManCou-H Containing Scaffolds

The ManCou-H containing scaffolds (figure 3.14 B) behaved similarly to the non-probe containing scaffolds in the case of the mesh morphology. The cells are clumped with no cellular orientation and increasing infiltration from day 1 to day 3. The cells on the mesh scaffolding look to be interacting with the fructose mimic but not actively metabolizing it. Cellular orientation on the ManCou-H containing aligned fibers matched that of the fibers on all days. Scaffold infiltration is high on day 1 decreasing on day 2 then increasing again by day 3. Cells appear spread out with almost no clumping on all days. Again, probe can be seen in the vicinity of the cells, but they do not appear to be taking them up. The cellular orientation on the honeycomb structures is visible on day 1, ManCou-H appears to be taken up by the fibroblasts on this day. The HDFa cells infiltrate the scaffold and maintain orientation on days 2 and 3.

3.5.2 184B5

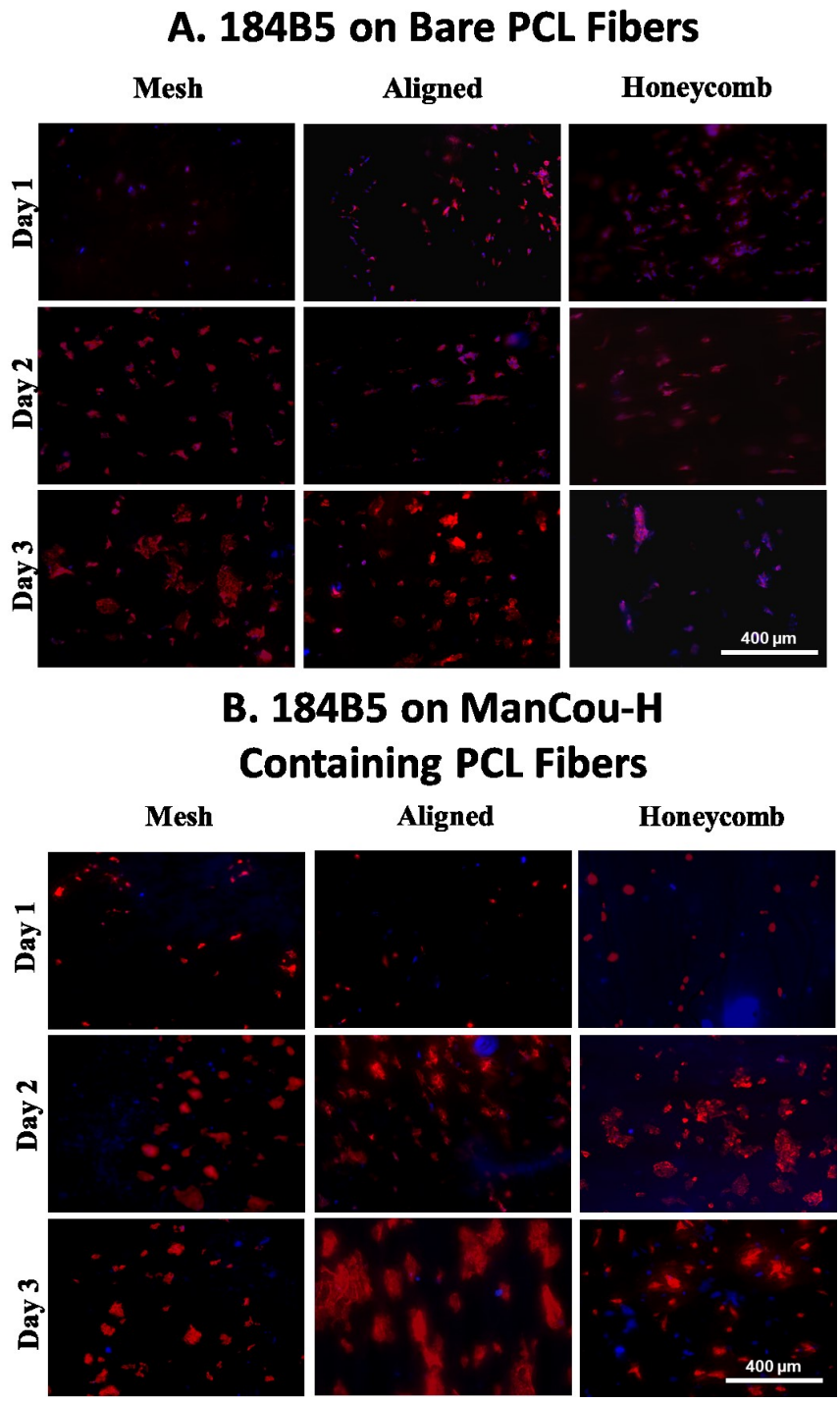

Figure 3.15 Fluorescent microscope images of healthy breast epithelium (184B5) on different morphologies of B) PCL scaffold with and A) without ManCou-H probe on days 1, 2 and 3. A) the nuclei were stained with DAPI (blue) B) the probe is in blue and the F-actin filaments were stained with Alexa Fluor® 594 Phalloidin (red). The overlapping of

the blue and red and dispersion by the fibers causes some of the cells to be seem pink in color. Images captured at 10X magnification.

3.5.2.1 184B5 on Bare Scaffolds

Figure 3.15A show images representative of the cell-cell and cell-scaffolds interactions of healthy breast epithelium, 184B5, on bare and ManCou-H containing scaffolds, respectively.

On the bare scaffolds the cells appeared to migrate and infiltrate all the scaffolds on day 1. Cells on mesh scaffolds appeared rounder and flatter on all days compared to more elongated and aligned morphologies on the honeycomb and aligned scaffolds. Infiltration of aligned and honeycomb scaffolds is at its highest on days 2 and 3. Little infiltration can be seen on the mesh scaffolds on all days. Clumping can be seen on day 3 among all scaffolds.

3.5.2.2 184b5 on ManCou-H Containing Scaffolds

Similar cell-cell and cell-scaffold interactions were observed on the ManCou-H containing scaffolds on day 1 (figure 3.15B). Clumping on the aligned and honeycomb scaffolds can be seen on day 2 and excessive clumping was exhibited on day 3 of the aligned scaffolds. The mesh fibers continued to exhibit round and flat cells but the elongated morphology of the cells on the aligned and honeycomb seen on the bare PCL was not as evident on the ManCou-H containing scaffolds.

3.5.3 MCF10AneoT

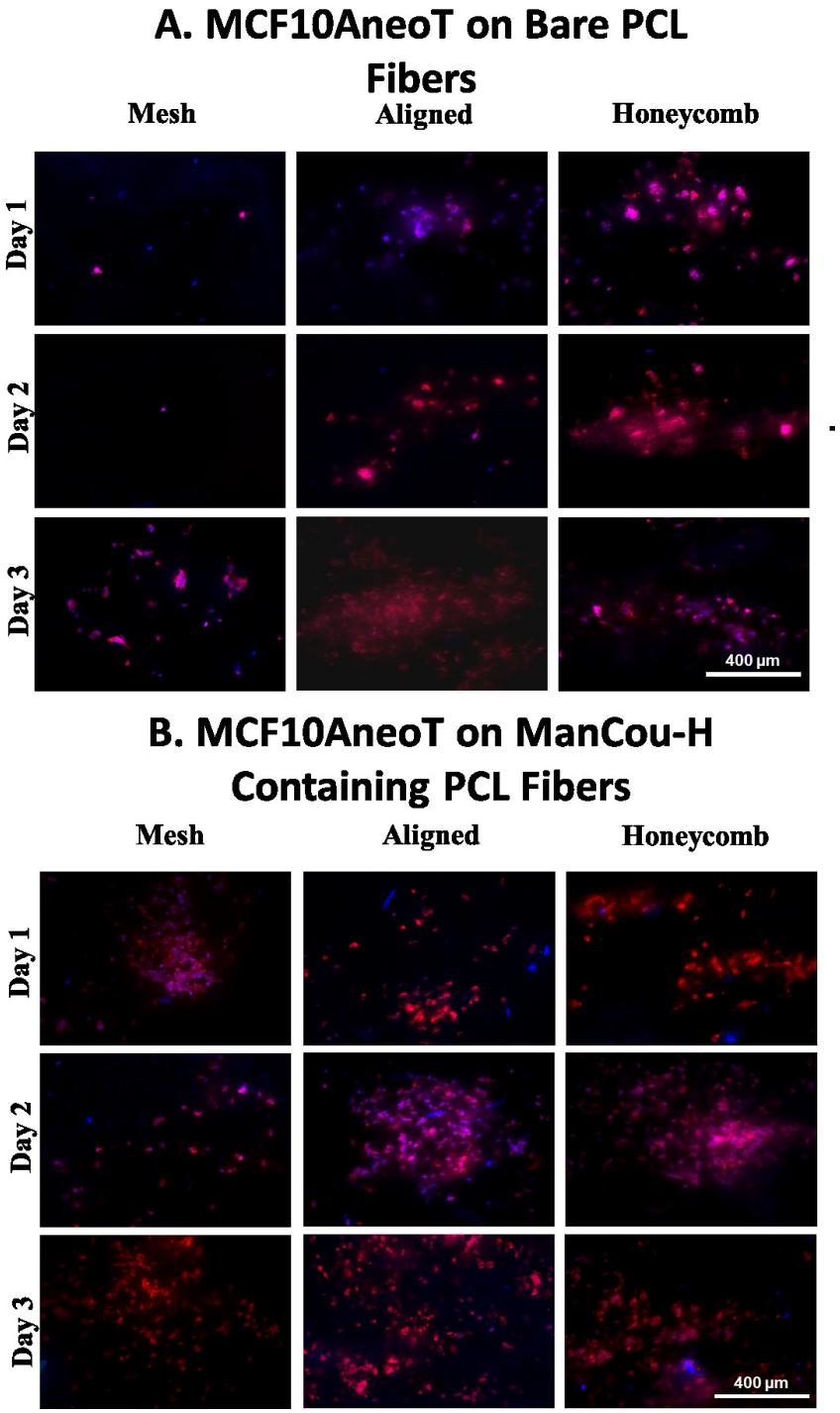

Figure 3.16 Fluorescent microscope images of Premalignant cells (MCF10AneoT) on different morphologies of B) PCL scaffold with and A) without ManCou-H probe on days 1, 2 and 3. A) the nuclei were stained with DAPI (blue) B) the probe is in blue and the F-actin filaments were stained with Alexa Fluor® 594 Phalloidin (red). The overlapping of

the blue and red and dispersion by the fibers causes some of the cells to be seem pink in color. Images captured at 10X magnification.

3.5.3.1 MCF10AneoT on Bare Scaffolds

The analysis of the cell-scaffold interaction of the premalignant cell line, MCF10AneoT, can be seen in figure 3.16A on bare scaffolds and ManCou-H containing scaffolds.

The cells on the bare scaffolds tended to clump together on all the morphologies on all the days. Cells appeared to clump in specific regions and maintained no cellular orientation on the mesh scaffolds. The aligned scaffolds exhibited cells which were spread across the scaffold with minimal alignment on days 1 and 2 then tended to clump on day 3. The cells on the honeycomb structure were able to infiltrate inside the different layers on day 1. This behavior could also be seen on day 2 in addition to some clumping. The cells again spread out by day 3 and continued to infiltrate the scaffold compared to days 1 and 2.

3.5.3.2 MCF10AneoT on ManCou-H Containing Scaffolds

The ManCou-H containing scaffold, figure 3.16B resulted in clumping on day 1 of the mesh scaffolds on days 2 and 3 the cells appeared to spread out and migrate to distant areas on the scaffold while showing rounded and flattened morphologies. Clumping was observed on day 2 on the aligned and honeycomb scaffolds. Probe uptake can be seen on days 1 and 2 of the mesh and aligned scaffolds and day 2 and 3 on the honeycomb fibers. Uptake was also seen on day 3 of the aligned scaffolds but to a lower extent. The mesh scaffolds showed cells which appeared to have a more spread out morphology among all days. Cells on aligned fibers aligned to the fibers to some extent on days 1 and 2 but became rounder by day 3. The honeycomb structures had cells which appeared both elongated and rounded at certain regions on all days with extensive scaffold infiltration.

3.5.4 MCF7

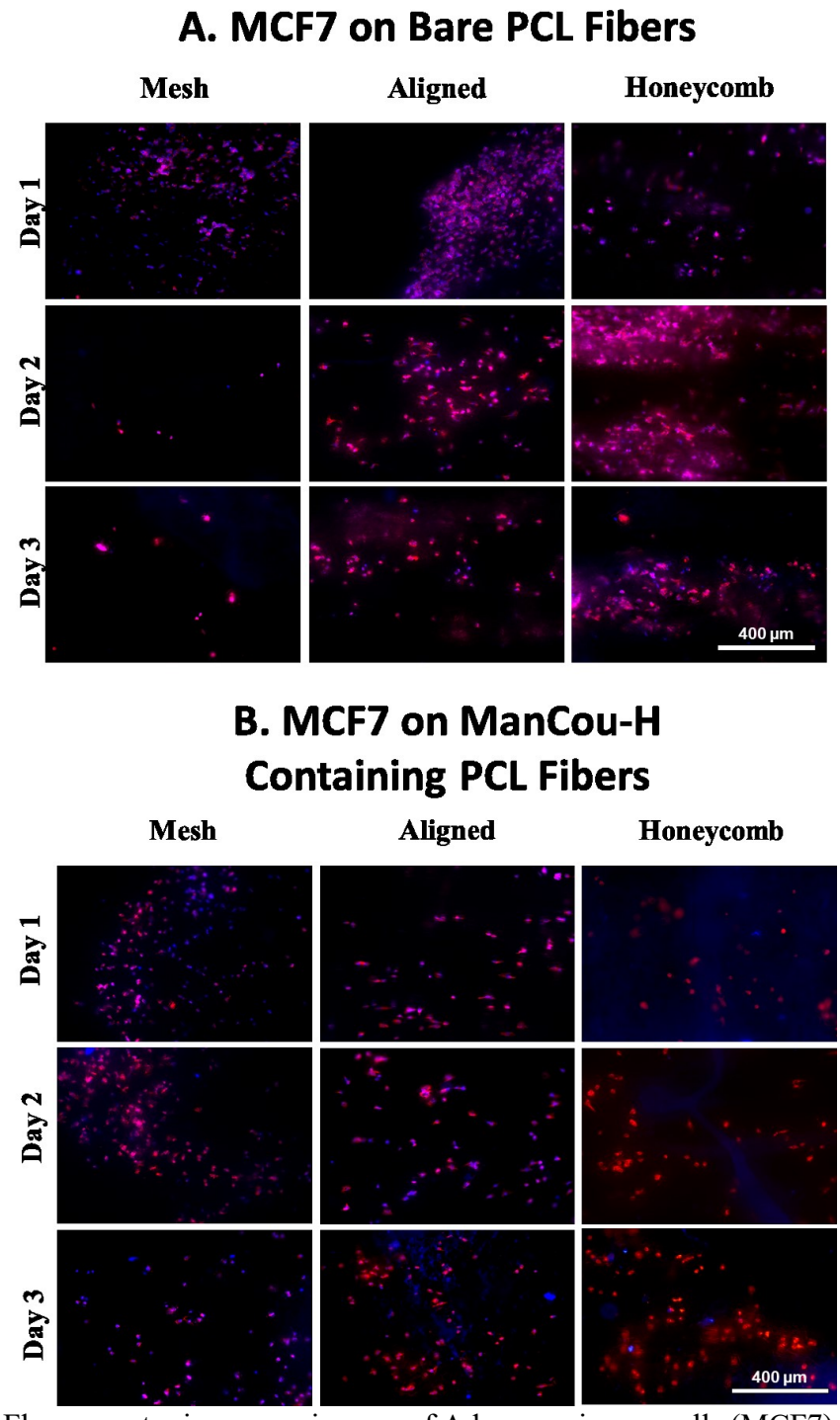

Figure 3.17 Fluorescent microscope images of Adenocarcinoma cells (MCF7) on different morphologies of B) PCL scaffold with and A) without ManCou-H probe on days 1, 2 and 3. A) the nuclei were stained with DAPI (blue) B) the probe is in blue and the F-actin filaments were stained with Alexa Fluor® 594 Phalloidin (red). The overlapping of the

blue and red and dispersion by the fibers causes some of the cells to be seem pink in color. Images captured at 10X magnification.

3.5.4.1 MCF7 on Bare Scaffolds

The behavior changes of the adenocarcinoma cell line, MCF7, due to the various morphologies as well as presence or absence of ManCou-H probe was qualitatively analyzed by staining the nucleus of cells on bare fibers and the cytoskeleton of all cells using immunofluorescent staining as was previously described.

Figure 3.17A illustrates the PCL fibers, these showed cells clumping on day 1 among all three morphologies but most extensive on the aligned scaffolds. The scaffolds with the mesh morphology showed cells on days 2 and 3 which were spread out and appeared to have infiltrated the scaffold, this made imaging difficult. The aligned scaffolds also showed cells spread out on days 2 and 3 however these cells showed an elongated morphology and were oriented along the direction of alignment of the fibers. The honeycomb scaffolds had a lot of cell clumping within the pores of the honeycomb and a very low concentration of cells on the boundary of the pores on day 2. On day 3 the cells on the honeycomb scaffold infiltrated the lower layers of the fibers and were present in between the fibers, this can be seen by the blurred regions between the fibers. Based on their distribution, morphology and orientation it appears the cells responded to the nano topographical cues provided by the different morphologies of each scaffold.

3.5.4.2 MCF7 on ManCou-H Containing Scaffolds

Similar trends can be deduced on the ManCou-H containing fibers in figure 3.17B. Probe uptake was observed on all days of the mesh and aligned scaffolds. Cells remained spread out with no clumping on any scaffold on any day. The mesh fibers had rounded cells whereas the aligned fibers had cells which aligned with the scaffold. The honeycomb scaffold showed no uptake of probe and cells varied from elongated alignment to more rounded morphology

3.5.5 MDA-MB-231

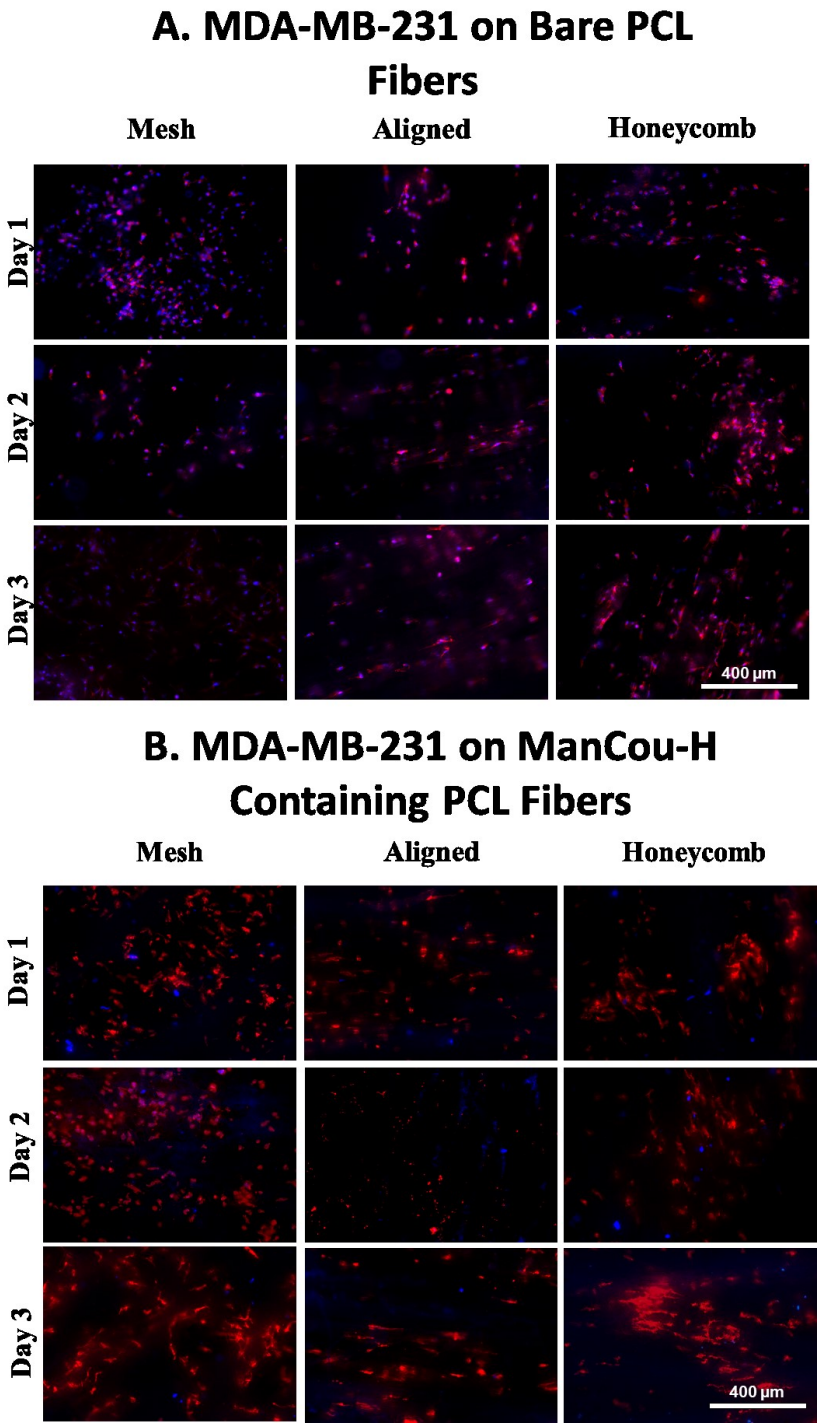

Figure 3.18 Fluorescent microscope images of triple negative adenocarcinoma (MDA-MB-231) on different morphologies of PCL scaffold with and without ManCou-H probe on days 1, 2 and 3. On the left the nuclei were stained with DAPI (blue) on the right the probe is in blue and the F-actin filaments were stained with Alexa Fluor® 594 Phalloidin (red).

The overlapping of the blue and red and dispersion by the fibers causes some of the cells to be seem pink in color. Images captured at 10X magnification.

3.5.5.1 MDA-MB-231 on Bare Scaffolds

Again, using immunofluorescent staining, the interaction between MDA-MB-231 cells and the bare scaffolds of different morphology were characterized (figure 3.18A).

On the mesh scaffolds the cells were distributed throughout without any logical orientation on days 1, 2 and 3. The cells on the bare aligned morphology lacked alignment on day 1 but were spread out across the sample, exhibiting little clumping. The cells on day 2 began to elongate and orient along the direction of fiber alignment. Cell infiltration into the different layers of the scaffolds can be deduced on day 3 by the blurred background. The bare honeycomb scaffolds exhibited little cellular alignment on day 1, but this was improved on day 2. By the third day in culture the cells infiltrated the scaffolds and attached to the walls of the honeycomb pores rather than the underlying layers of the fibers. Surprisingly, none of the morphologies seemed to promote clumping together of cells.

3.5.5.2 MDA-MB-231 on ManCou-H Containing Scaffolds

On the ManCou-H containing scaffolds, figure 3.18B, the triple negative adenocarcinoma (MDA-MB-231) remained fairly spread out along the scaffold, only showing slight clumping on day 1 of the honeycomb scaffold. Probe uptake can be seen on day 2 of the mesh scaffolds. The cells appear to have detached from the aligned scaffolds on day 2 otherwise maintaining an elongated morphology oriented along and infiltrated within the scaffold. The mesh scaffolds exhibited rounded cells on day 1 and 2 but elongated unoriented cells on day 3. The honeycomb fibers have cells oriented along the fibers with cells exhibiting both elongated and somewhat rounded cells.

3.6 Cell alignment

3.6.1 Cell Alignment on Bare PCL scaffolds

The deviation of the fibroblasts on the scaffolds of all morphologies was as expected (figure 3.19A), a high deviation in orientation among the mesh scaffolds and more alignment, less deviation on the honeycomb and aligned morphologies. This trend was seen for days 1 and 2 however alignment on the mesh scaffolds on day 3 appears to be nearly equivalent to that of the honeycomb and aligned scaffolds, this is likely due to an error in segmentation. The healthy breast epithelium showed the lowest deviation among the honeycomb samples across all days with the mesh and aligned scaffold showing similar behavior (figure 3.19B).

Looking at the premalignant cell line the orientation deviation among the cells appears to be uniform among all samples except the mesh scaffolds on day 2 which only shows one cell and resulting in a deviation in orientation from other cell lines of 0 (figure 3.19C). The adenocarcinoma shows similar trends with the lower deviation in cell orientation among cells on aligned and honeycomb structures (figure 3.19D). MDA-MB-231 appears to be quite variable, showing better alignment on the honeycomb structure on day 1 and aligned on day 2 and 3 (figure 3.19E). Additional segmentation methods may need to be implemented in order to get a better picture of what is happening when cells have clumped.

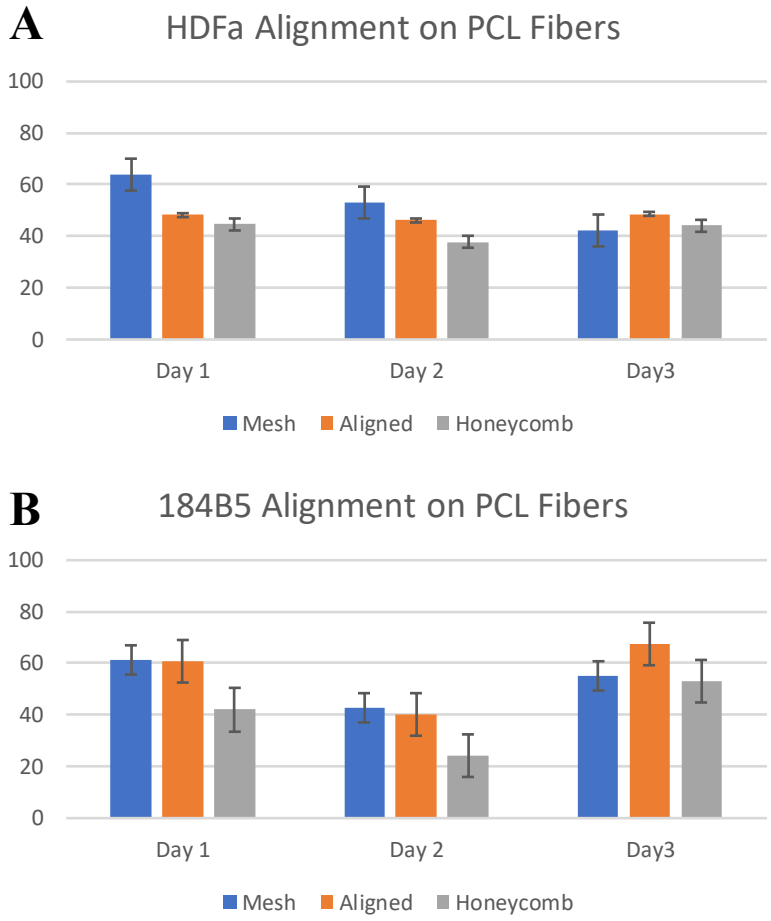

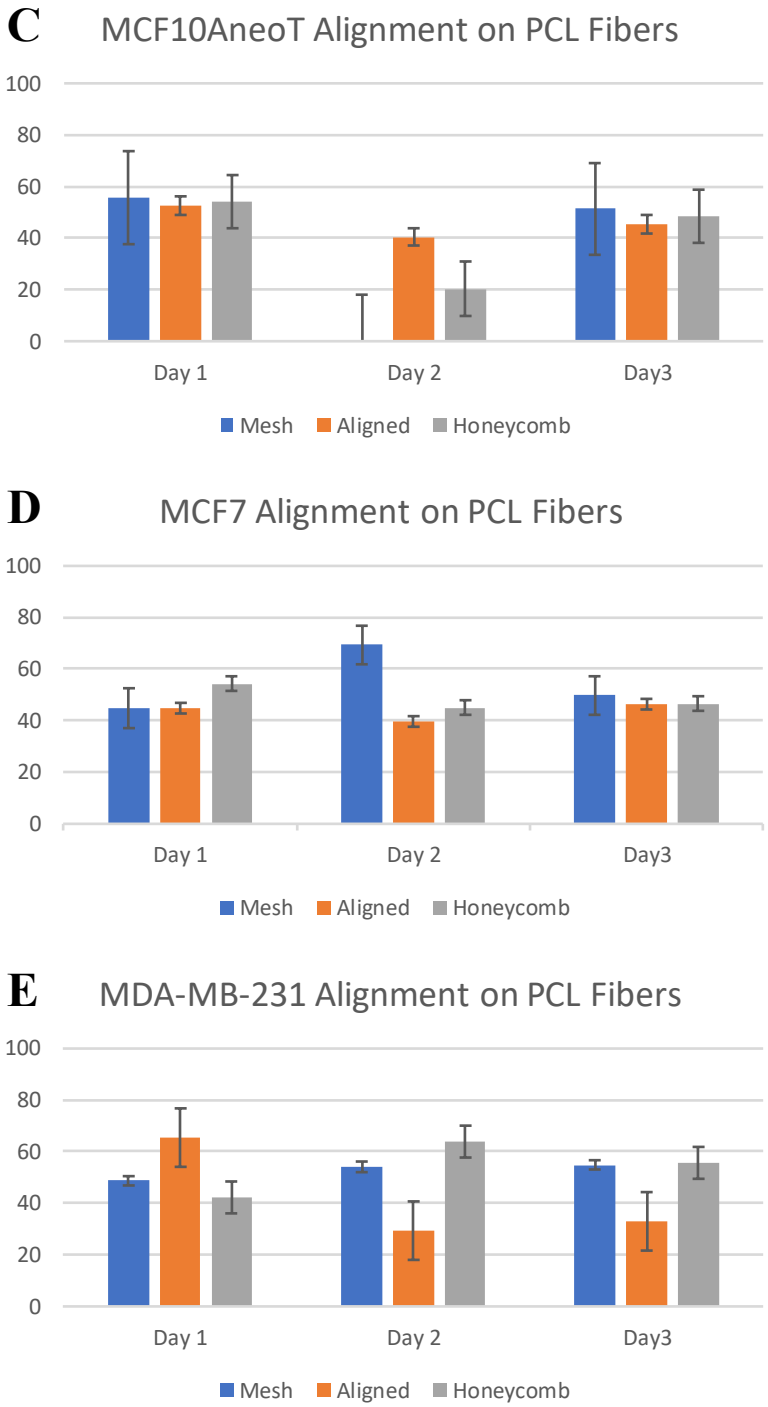

Figure 3.19 Cell orientation deviation of all cell lines on all bare morphologies for days 1. 2 and 3. Results were obtained by averaging the directional deviation between cells given by two different segmentation methods, watershed and Otsu thresholding. The y axis represents the deviation from the mean orientation of the cells on the scaffolds.

3.6.2 Cell Alignment on ManCou-H Containing PCL scaffolds

Orientation deviation among the HDFa cell line was minimized on days 2 and 3 on the aligned fibers (figure 3.20A). The honeycomb structures showed the least deviation on day 1 but the highest deviation on day 3. These results are nearly opposite to those shown by 184B5 which had the least deviation among the mesh scaffolds on days 1 and 2, the highest deviation of the honeycomb structures on days 1 and 2 and the lowest deviation on day 3 (figure 3.20B). The aligned scaffolds showed the highest deviation on day 3. For the premalignant cell line, the aligned scaffolds exhibited slightly less deviation among cell orientation, but deviation is very similar among all morphologies (figure 3.20C). The adenocarcinoma behaved as would be expected, showing the lowest deviation among the cells seeded in the aligned fibers followed by the cells on honeycomb fibers and the highest deviation on the mesh scaffolds on all days (figure 3.20D). Like the bare scaffolds the MDA-MB-231 behaved variably among all scaffolds, the aligned showed the lowest deviation on days 1 and 3 (figure 3.20E). Mesh showed the lowest on day 2 and the highest on day 3.

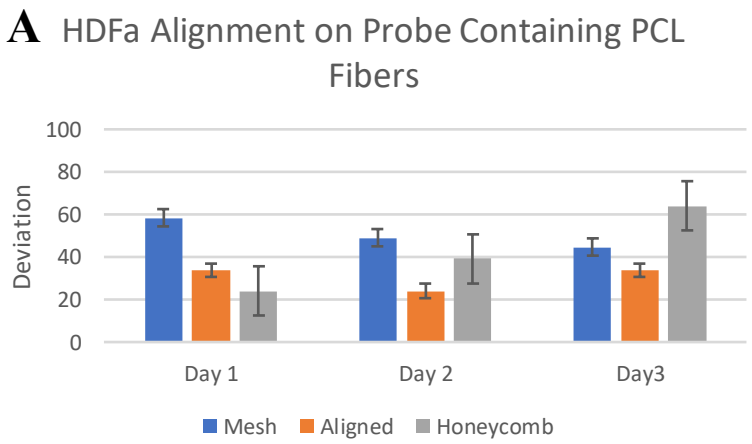

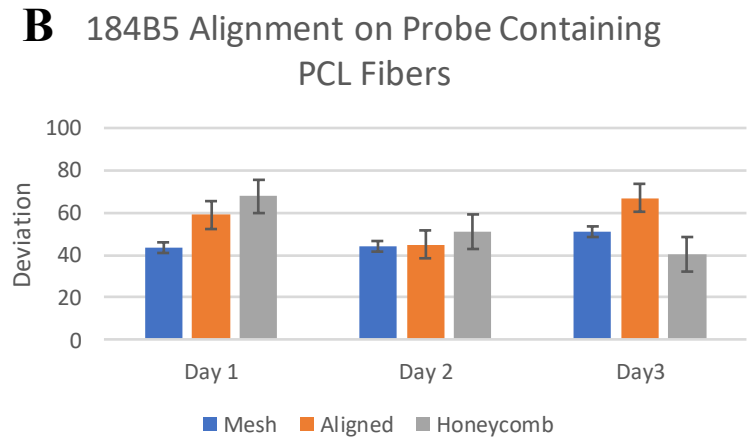

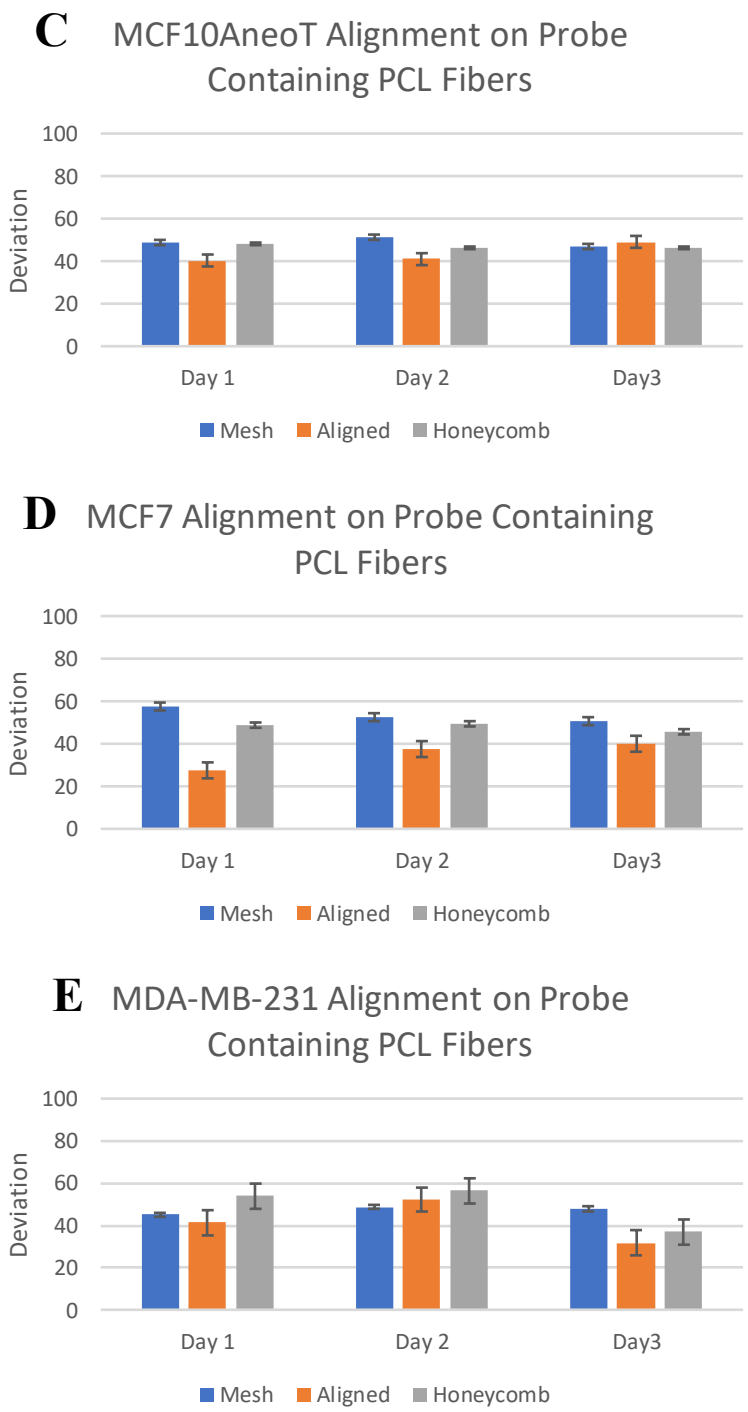

Figure 3.20 Cell orientation deviation of all cell lines on all ManCou-H containing morphologies for days 1. 2 and 3. Results were obtained by averaging the directional deviation between cells given by two different segmentation methods, watershed and Otsu thresholding. The y axis represents the deviation from the mean orientation of the cells on the scaffolds.

3.7 Cell Viability

3.7.1 Cell Viability on Bare Scaffolds

The cell viability of each cell line on the scaffolds at time points 1, 2 and 3 days was characterized by the reduction of resazurin to resorufin.

On the bare PCL scaffolds, the human dermal fibroblasts exhibited a significant preference towards the mesh scaffolds peaking at day 1 then appearing to have a lower metabolic activity on day 2 before increasing again on day 3 (figure 3.21A). These cells otherwise showed an increase in cell number among all other morphologies among all days. The difference in increased cell number with each day on aligned morphology was non-significant across all the days. The healthy breast epithelium showed an increase in cell number across all morphologies of the scaffolds on all the days (figure 3.21B). The difference in increased cell number with each day on aligned and honeycomb morphologies was non-significant across all the days. Scaffolds also demonstrated a significant increase in cell number among the adenocarcinoma cell line, MCF7, could be seen across all morphologies of the scaffold on all days (figure 3.21D). Day 3 showed a lower relative number of viable cells on the positive control when compared to the bare PCL morphologies. The difference in increased cell number with each day on positive control was non-significant across all the days. MDA-MB-231 cells exhibited a statistically significant increase in cell viability over all the days on all the samples (figure 3.21E). However, the positive control was the most favorable substrate for the triple negative cell line when compared to the other morphologies. This is likely due to the stiffness of the positive control, a tissue culture plate, ~10 GPa, which plays a major role in cellular viability as shown by Mah and colleagues [53]. MCF10AneoT showed less uniform cell viability when compared to the viabilities of MDA-MB-231 and MCF7 cell lines on all morphologies (figure 3.21C). A more pronounced increase in cell number is seen from day 1 to day 2 on the mesh and aligned scaffolds. However, only an increase from day 2 to day 3 on the honeycomb scaffolds was shown to be significant. The positive control had non-significant changes in cell viability among MCF10AneoT cells. The uniform behavior of the MDA-MB-231 and MCF7 cell lines is present among all morphologies exhibiting an increase in cell number for all three days.

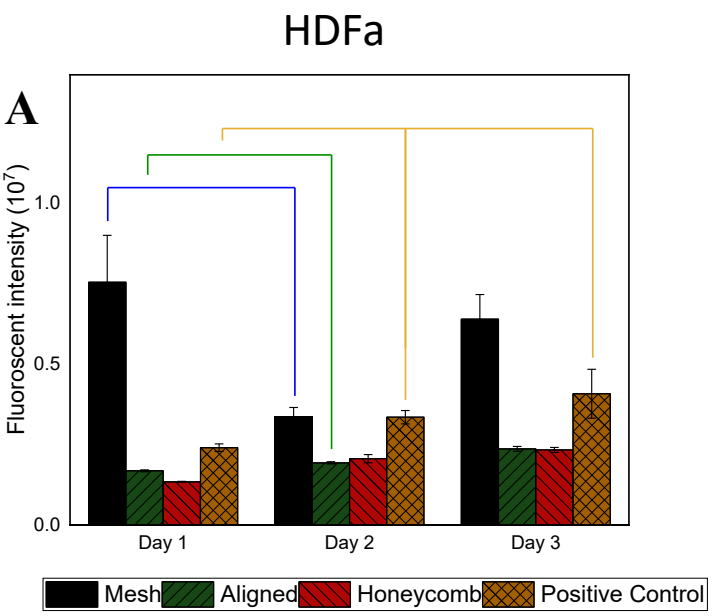
HDFa
A
Fluoroscent intensity (10^7)
1.0
0.5
0.0
Day 1
Day 2
Day 3
Mesh
Aligned
Honeycomb
Positive Control

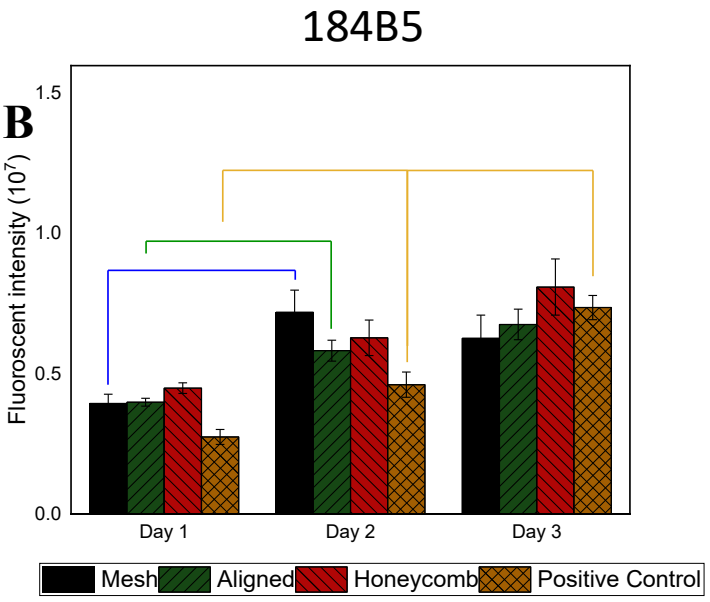
184B5
B
Fluoroscent intensity (10^7)
1.5
1.0
0.5
0.0
Day 1
Day 2
Day 3
Mesh
Aligned
Honeycomb
Positive Control

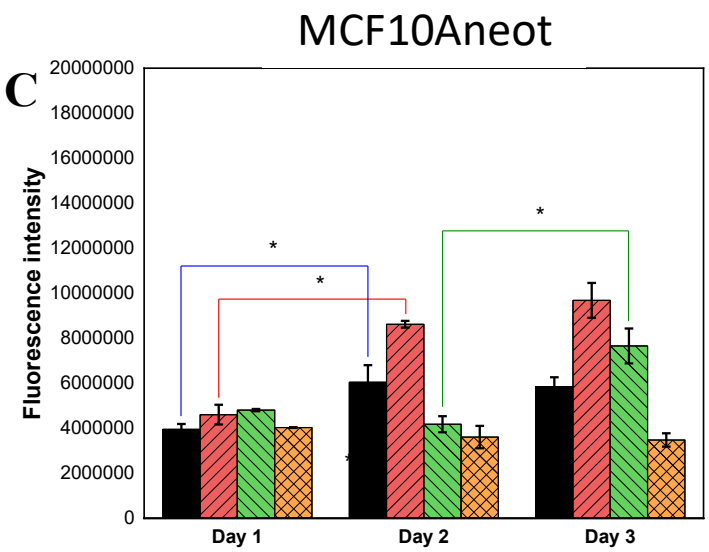
C
MCF10Aneot
Fluorescence intensity
20000000
18000000
16000000
14000000
12000000
10000000
8000000
6000000
4000000
2000000
0
Day 1
Day 2
Day 3
*
*
*

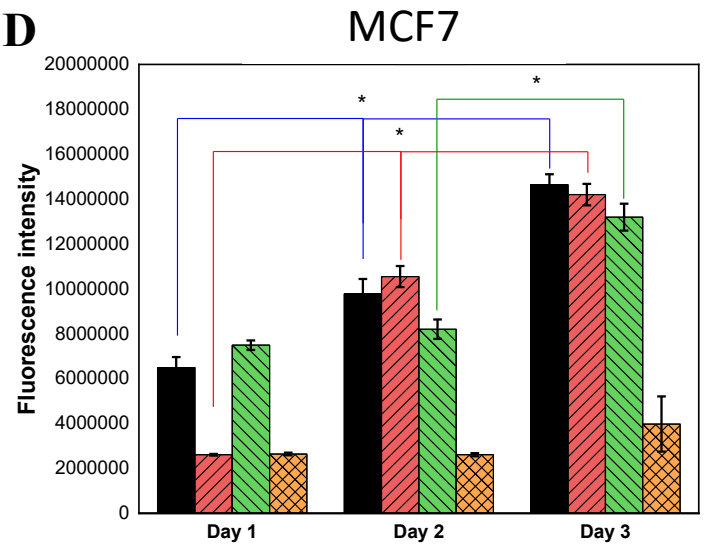
D
MCF7
Fluorescence intensity
20000000
18000000
16000000
14000000
12000000
10000000
8000000
6000000
4000000
2000000
0
Day 1
Day 2
Day 3
*
*
*

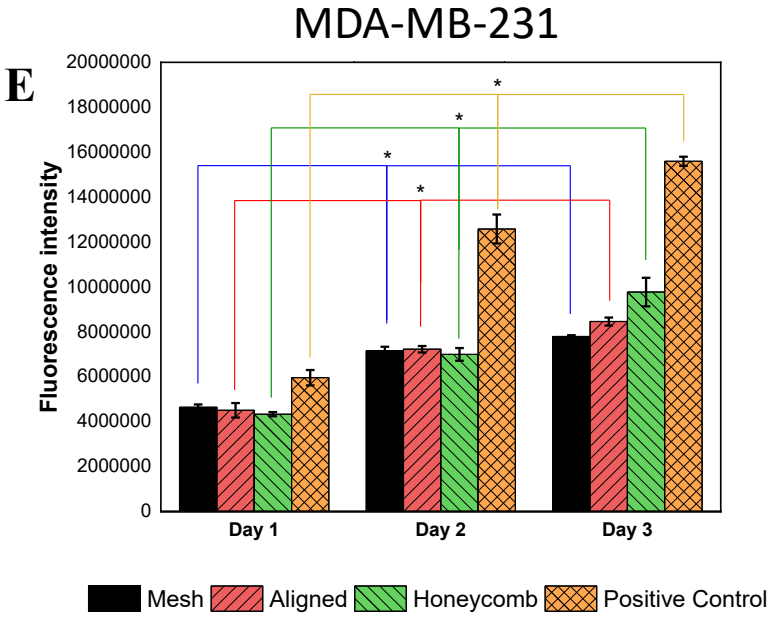

Figure 3.21 Quantification of cell viability of bare scaffolds on days 1, 2 and 3 on different bare morphologies and cell lines. A) Cell viability of HDFa (Human Dermal Fibroblast) cells on different morphologies of the scaffold. B) Cell viability of 184B5 (healthy breast epithelium) cells on different morphologies of the scaffold. C) Cell viability of MCF10AneoT (premalignant) cells on different morphologies of the scaffold. D) Cell viability of MCF7 (adenocarcinoma) cells on different morphologies of the scaffold. Cells seeded on mesh scaffold had a significant increase in cell number till day 3. E) Cell viability of MDA-MB-231 (triple negative) cells on different morphologies of the scaffold. The cell number increased consistently on all scaffolds till day 3. The increase in cell viability was inconsistent across any morphology. Error bars represent the standard error of mean and statistical significance is indicated by p values (*$p<0.05$)

3.7.2 Cell Viability on ManCou-H Containing Scaffolds

On the ManCou-H containing PCL scaffolds, the HDFa again had a high cell number on day 1 which dropped on day 2 only to significantly increase again by day 3. The aligned fibers also showed a significant increase in cell viability among all days while the honeycomb structures only offered a significant increase between days 1 and 2 (figure 3.22A). The healthy breast epithelium showed an increase in cell number across all morphologies of the scaffolds on all the days (figure 3.22B) indicating a slight preference towards the aligned morphology but no significant changes were seen between any morphology or any day. The premalignant cell line showed a similar drop in viability on the mesh fibers from day 1 to day 2 as HDFa but to a lesser extent (figure 3.22C). A significant increase in cell viability across all days was seen on the aligned scaffolds. The mesh and honeycomb scaffolds had a significant increase in cell proliferation from days 2 to 3 with what would appear to be an overall preference towards the honeycomb

structure. An increase among all morphologies over all 3 days can be seen in the adenocarcinoma cell line (figure 3.22D). This increase is significant for mesh and aligned scaffolds among all days but only for days 2 to 3 for the honeycomb morphology. The MCF7 appeared to prefer the mesh scaffolds to any other topography. An increase in MDA-MB-231 cell number can again be seen across all morphologies for the 3-day study. This increase is significant in the mesh scaffolds from day 1 to day 2 and from day 2 to day 3 on the honeycomb and aligned morphologies (figure 3.22E).

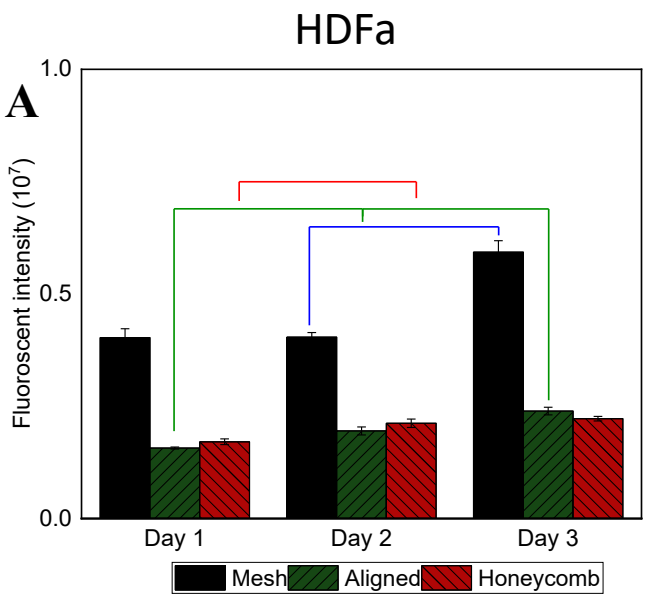
HDFa
A
1.0
0.5
0.0
Fluoroscent intensity (10^7)
Day 1
Day 2
Day 3
Mesh
Aligned
Honeycomb

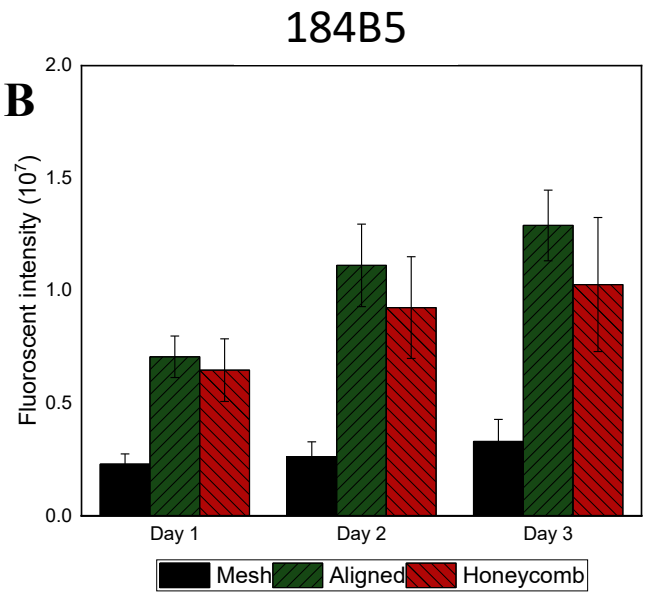
184B5
B
2.0
1.5
1.0
0.5
0.0
Fluoroscent intensity (10^7)
Day 1
Day 2
Day 3
Mesh
Aligned
Honeycomb

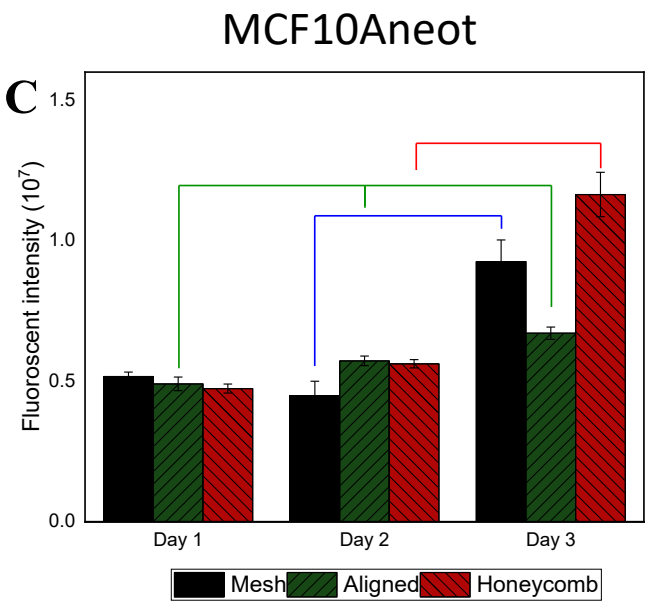
MCF10Aneot
C
1.5
1.0
0.5
0.0
Fluoroscent intensity (10^7)
Day 1
Day 2
Day 3
Mesh
Aligned
Honeycomb

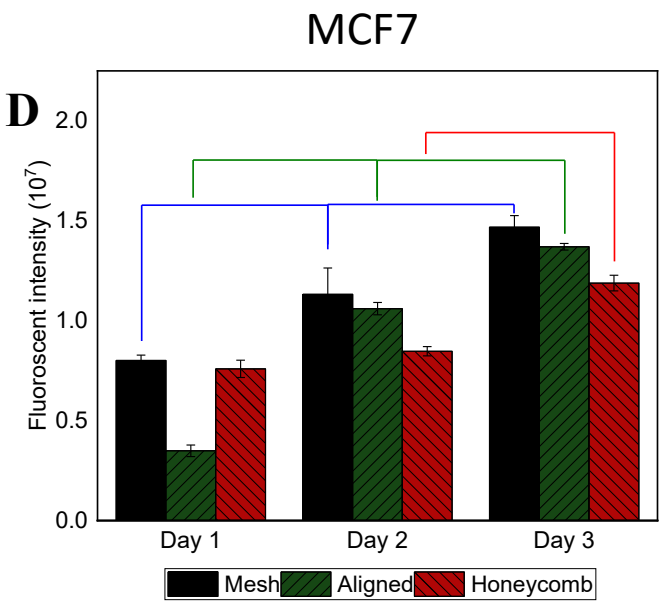
MCF7
D
2.0
1.5
1.0
0.5
0.0
Fluoroscent intensity (10^7)
Day 1
Day 2
Day 3
Mesh
Aligned
Honeycomb

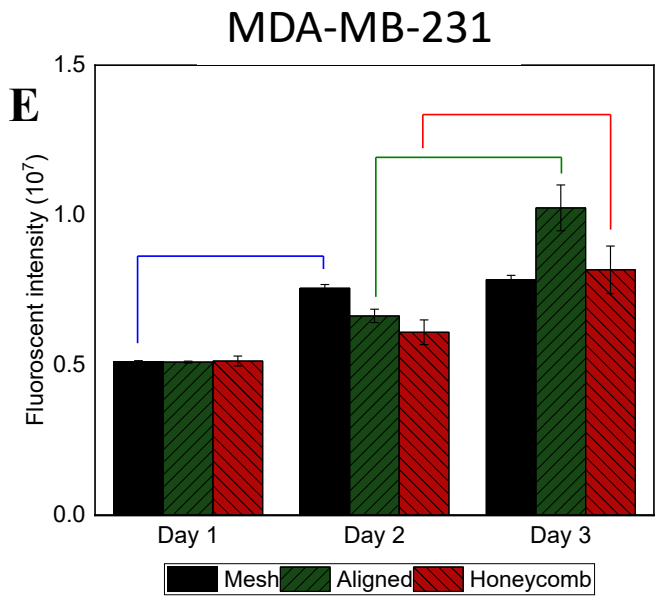

Figure 3.22 Quantification of cell viability of ManCou-H containing scaffolds on days 1, 2 and 3 on different morphologies and cell lines. A) Cell viability of HDFa (Human Dermal Fibroblast) cells on different morphologies of the scaffold. B) Cell viability of 184B5 (healthy breast epithelium) cells on different morphologies of the scaffold. C) Cell viability of MCF10AneoT (premalignant) cells on different morphologies of the scaffold. D) Cell viability of MCF7 (adenocarcinoma) cells on different morphologies of the scaffold. Cells seeded on mesh scaffold had a significant increase in cell number till day 3. E) Cell viability of MDA-MB-231 (triple negative) cells on different morphologies of the scaffold. The cell number increased consistently on all scaffolds till day 3. The increase in cell viability was inconsistent across any morphology. Error bars represent the standard error of mean and statistical significance is indicated by p values (*$p<0.05$)

3.8 Discussion

Topographical features and mechanical properties of the scaffolds were shown to influence the cell viability, cell-cell interaction and cell-scaffolds behavior. The adenocarcinoma, MCF7, cells proliferated well in all tested without much preference towards any particular topographical morphology. These findings are supported by the work of Chaudhuri et al. on the inhibition of Rho-ROCK-Myosin signaling in malignant cells leading to the proliferation of adenocarcinoma irrespective of the topography [23]. The cells did tend to prefer elastomeric scaffolds with low Young's modulus and stiffness such as the mesh scaffolds over scaffolds with higher Young's modulus and stiffness like the honeycomb and positive control. This agrees with several experimental investigations on MCF7 including Li et. al on the mechanical properties of breast cancer cells through atomic force microscopic measurements and [54] and durotaxis studies performed by Cavo et. al [55].

Alternatively, the triple-negative cell line tended to thrive on scaffolds with a stiffer matrix, this was expected due to the regulation of the YAP (Yes associated protein)/TAZ (transcriptional coactivator with PDZ-binding motif) followed by the activation of the Hippo cascade [56]. Topotactic and durotactic gradients guided the cellular alignment and infiltration on the honeycomb and aligned scaffolds which demonstrated extensive cellular infiltration as well as alignment. Lin et. al reported the stiffness of scaffolds positively enhances the migration potential of metastatic cells [57] and can drive tumor progression through a TWIST1-G3BP2 mechanotransduction pathway [58]. The premalignant cells preferred the aligned scaffolds as they appeared to allow the cells to infiltrate and orient along the fibers. The aligned fibers provide topographical cues which aid in the cell spreading due to migration and can also impact tumor progression and metastasis [59].

A certain amount of cell clumping was reported on all morphologies, this is in direct correlation of the metastatic potential of the cells. The metastatic potential of the cells indicates the clumped cells form protrusions followed shortly after by invasion [60, 61]. Observations made by Rubashkin et. al are consistent with increased viability and spreading of premalignant cells in stiffer scaffolds [62].

Additionally, there did not appear to be much preferential difference in cell attachment, migration or proliferation between ManCou-H and non ManCou-H containing scaffolds. With the lack of nutrition offered by the fructose mimic it was expected that the cancerous cell lines would take up the probe via GLUT5 and die off. Alterations in this expectation could be due to the minimal amount of probe released in such a short time as shown by the degradation studies. The optimal concentration of ManCou-H within the scaffold may yet need to be determined.

For these reasons, it can be concluded that the cells respond to changes in scaffolds topography and mechanical properties based on the stage of cancer.

This indicates an *in vitro* tumor model which takes topotaxis and durotaxis into account would be suitable. Such a scaffold can provide the ideal platform for studying breast cancer metastasis or for localized therapy to inhibit the growth of metastatic cells. The efficient electrospun scaffold design also allows the scaffold system to be easily adapted for the study and treatment of other cancers through the respective topotactic gradients [63].

4 Conclusion

Different topotaxic and durotaxic features can be incorporated into 3D scaffolds via Polycaprolactone (PCL) electrospinning. These scaffolds have been shown to have similar surface chemistry yet when cancer cell lines of various malignancies were seeded behavior changes were apparent. Adenocarcinoma, triple negative, and premalignant breast cancer cell lines were seeded on nanofiber scaffolds of different morphologies in the presence and absence of fluorescent fructose mimics, ManCou-H. Using healthy breast epithelium and human dermal fibroblasts as controls, the cell-cell and cell-scaffold interactions were qualitatively analyzed using immunofluorescent staining and quantitatively analyzed for their cell viability over a period of 3 days.

Human dermal fibroblasts proliferated more highly on mesh scaffolds followed closely by the positive control, both which exhibited a low elastic modulus. This was the case in the presence and absence of the ManCou-H probe. Cell alignment to the scaffold appeared to be more prevalent in the fibroblasts compared to other cell lines. Cells showed favorable alignment along these scaffolds. The adenocarcinoma cells also proliferated more highly on mesh scaffolds which exhibited a low elastic modulus similar to the HDFa.

Healthy breast epithelium showed high variability, not seeming to prefer any one morphology on the bare fibers yet showing preference to the higher stiffness of the aligned and honeycomb structures. Despite these preferences the cells still appeared to have little alignment due to excessive clumping. The premalignant cell line preferred a more aligned morphology which had a high stiffness and more contact guidance when on PCL scaffolds without the ManCou-H. In the presence of ManCou-H this preference shifted more towards the honeycomb morphology which exhibited slightly less contact guidance.

For PCL fibers which did not contain ManCou-H the triple negative cell line appeared to exhibit a slight preference to the honeycomb scaffolds with higher and strength as indicated by the cell viability as well as the immunofluorescent staining. In the presence of the ManCou-H, MDA-MB-231 appeared to shift its preference to the aligned morphology with the mesh and honeycomb not far behind.

It was found that these scaffolds were able to mimic the mechanical and topographical tumor microenvironment by providing biophysical signals for topotaxis and durotaxis. These scaffolds were also able to provide information on the molecular uptake behavior of cells on various topographies. Changes in uptake altered the cell-cell and cell-scaffold interactions on similar topographies.

It was also noted that the cancerous cell lines aligned more readily with the aligned scaffolds by day 3 on the bare PCL scaffolds, when compared to the non-cancerous controls. This trend was not the same in the presence of the ManCou-

H probe. The cancerous cell lines still showed a high alignment to the aligned scaffolds on day 3 but to a much smaller capacity. The MCF10ANeot showed similar deviation among all scaffolds. Furthermore, the HDFa exhibited high alignment on day 3 of the aligned scaffolds in the presence of the probe compared to the absence.

These differential preferences towards topographical features indicate not only the benefit of using nanofiber scaffolds as platforms to model breast cancer but also the feasibility to design a nanofiber scaffold capable of attracting and trapping metastasizing cancer cells. Further studies will also be done to optimize the probe concentration within the scaffolds to offer a better understanding for the slow release of drugs or chemokines from PCL platforms.

5 Future Work

Protein analysis through western blot would indicate what is happening within the cell with regards to upregulation and downregulation of specific pathways. Further investigation into preferences of different cancer cell lines such as small cell carcinoma, and kidney cancer would allow for potential expansion into relevance in all cancers. All of this research is currently underway to potentially lead to an engineered scaffold with controllable stiffness, structure and shape, in order to combat cancerous cells within the body as a cancer trap or outside of the body as a research platform for multiple types of cancer.

Based on the response observed for cancer cells on scaffolds with the fructose-like molecular probe, the concentration, availability and the time of cell interaction with the probe should be optimized. Since there is also a cell-line dependent preference towards scaffolds, the probe optimization will also need to incorporate scaffold morphology. Future studies will include direct comparison with fructose in the scaffolds.

6 Appendix

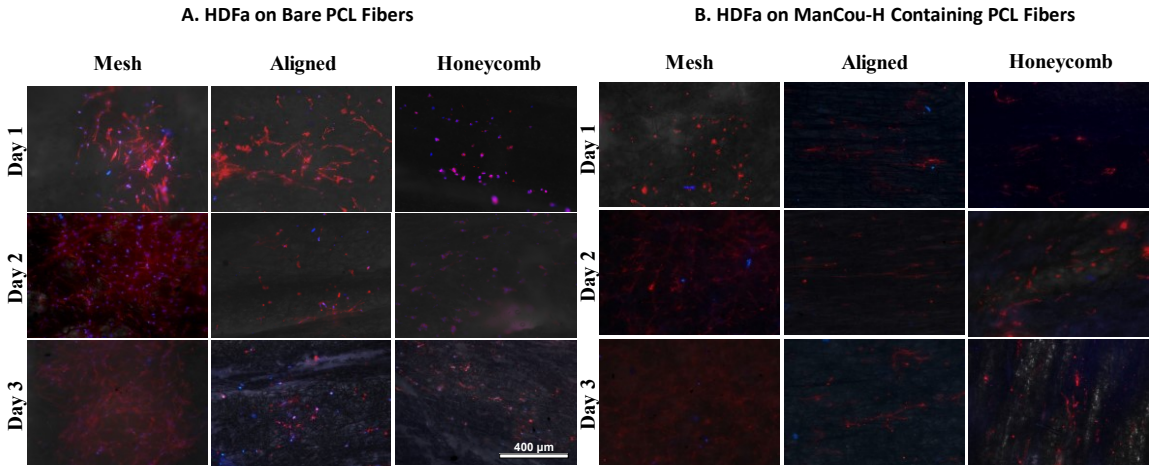

Figure 6.1 Fluorescent microscope images of human dermal fibroblasts (HDFa) on different morphologies of the PCL scaffold with and without ManCou-H probe on days 1, 2 and 3. In A) the nuclei were stained with DAPI (blue) in B) the probe is in blue and the F-actin filaments were stained with Alexa Fluor® 594 Phalloidin (red). The images were overlaid with the phase contrast image to provide additional information about the scaffold morphology. The overlapping of the blue and red and dispersion by the fibers causes some of the cells to be seen pink in color. Images captured at 10X magnification.

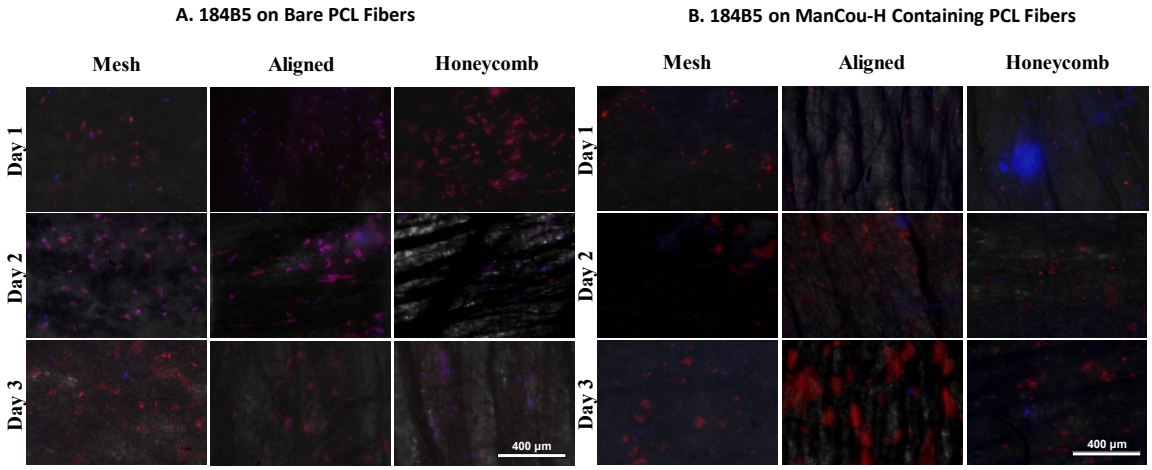

Figure 6.2 Fluorescent microscope images of healthy breast epithelium (184b5) on different morphologies of the PCL scaffold with and without ManCou-H probe on days 1, 2 and 3. In A) the nuclei were stained with DAPI (blue) in B) the probe is in blue and the F-actin filaments were stained with Alexa Fluor® 594 Phalloidin (red). The images were overlaid with the phase contrast image to provide additional information about the scaffold morphology. The overlapping of the blue and red and dispersion by the fibers causes some of the cells to be seen pink in color. Images captured at 10X magnification.

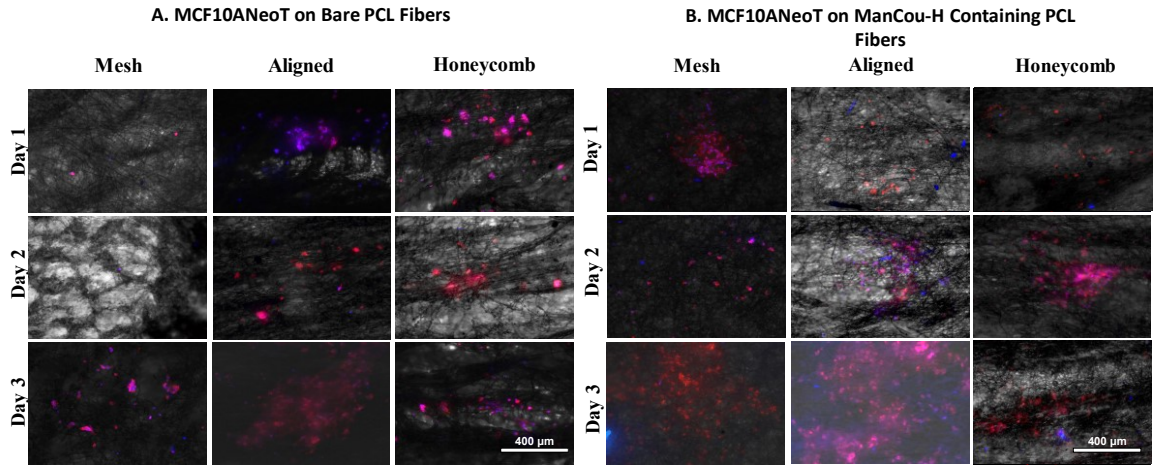

Figure 6.3 Fluorescent microscope images of premalignant breast cancer cells (MCF10AneoT) on different morphologies of the PCL scaffold with and without ManCou-H probe on days 1, 2 and 3. In A) the nuclei were stained with DAPI (blue) in B) the probe is in blue and the F-actin filaments were stained with Alexa Fluor® 594 Phalloidin (red). The images were overlaid with the phase contrast image to provide additional information about the scaffold morphology. The overlapping of the blue and red and dispersion by the fibers causes some of the cells to be seen pink in color. Images captured at 10X magnification.

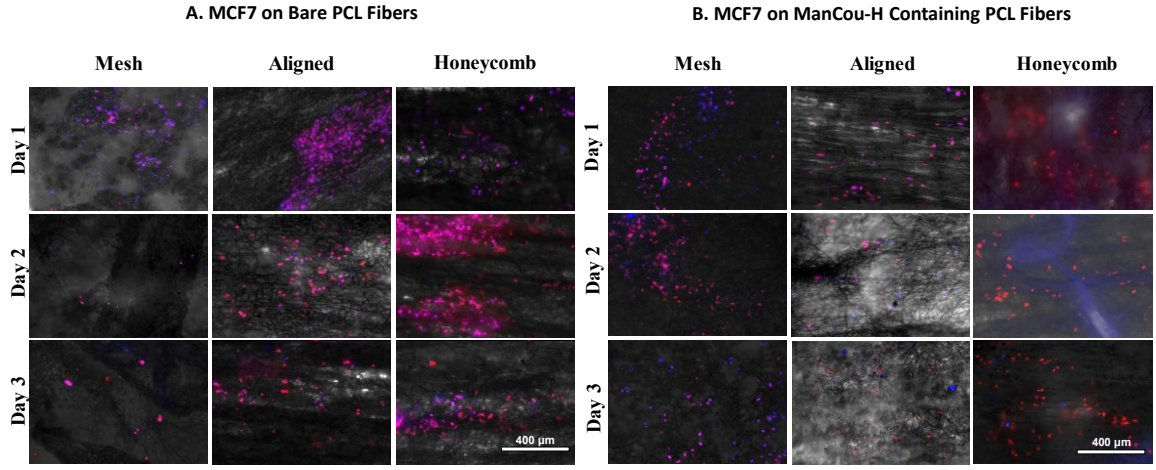

Figure 6.4 Fluorescent microscope images of adenocarcinoma cells (MCF7) on different morphologies of the PCL scaffold with and without ManCou-H probe on days 1, 2 and 3. In A) the nuclei were stained with DAPI (blue) in B) the probe is in blue and the F-actin filaments were stained with Alexa Fluor® 594 Phalloidin (red). The images were overlaid with the phase contrast image to provide additional information about the scaffold morphology. The overlapping of the blue and red and dispersion by the fibers causes some of the cells to be seen pink in color. Images captured at 10X magnification.

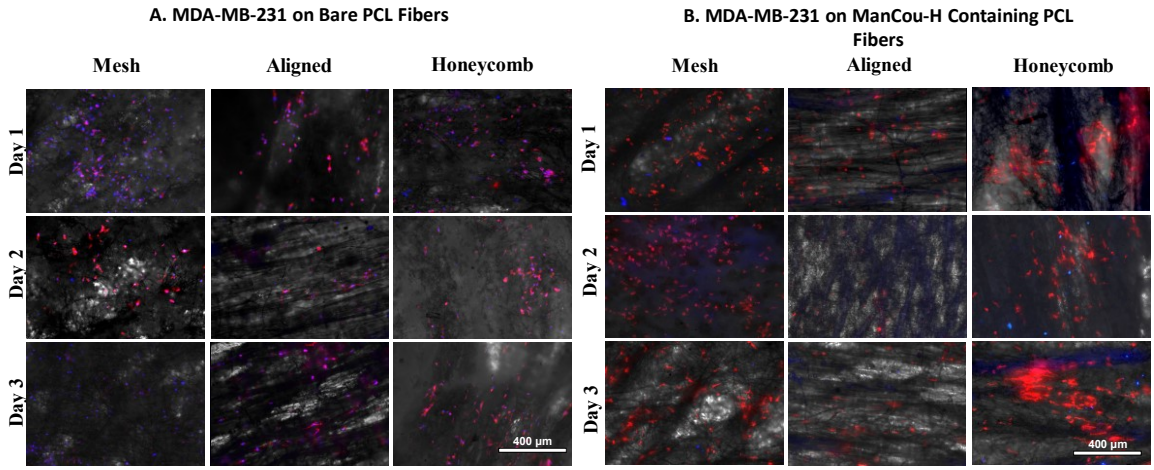

Figure 6.5 Fluorescent microscope images of triple negative adenocarcinoma cells (MDA-MB-231) on different morphologies of the PCL scaffold with and without ManCou-H probe on days 1, 2 and 3. In A) the nuclei were stained with DAPI (blue) in B) the probe is in blue and the F-actin filaments were stained with Alexa Fluor® 594 Phalloidin (red). The images were overlaid with the phase contrast image to provide additional information about the scaffold morphology. The overlapping of the blue and red and dispersion by the fibers causes some of the cells to be seen pink in color. Images captured at 10X magnification.

7 Reference List

1. SEER. *Cancer Stat Facts*. 2020 [cited 2020, March 5]; Available from: https://seer.cancer.gov/statfacts/.
2. SEER. *Cancer Stat Facts: Common Cancer Sites*. 2020 [cited 2020 March 5]; Available from: https://seer.cancer.gov/statfacts/html/common.html.
3. Surveillance, E.a.E.R.P. *Cancer Stat Facts: Female Breast Cancer*. 2020 March 5, 2020]; Available from: https://seer.cancer.gov/statfacts/html/breast.html.
4. SD, C.J.R.J.P., *The costs of treating breast cancer in the US: a synthesis of published evidence.* 2009. **27**(3): p. 199-209.
5. Petrek, J.A., et al., *Incidence, time course, and determinants of menstrual bleeding after breast cancer treatment: a prospective study.* 2006. **24**(7): p. 1045-1051.
6. Organization, W.H. *Cancer*. 2015 [cited 2020, March 1]; Available from: https://www.who.int/topics/cancer/en/.
7. Society, A.C. *What Is Cancer?* 2015 [cited 2020 February 4]; Available from: https://www.cancer.org/cancer/cancer-basics/what-is-cancer.html.
8. Foundation, N.B.C. *Stages*. 2019 [cited 2020, March, 1]; Available from: https://www.nationalbreastcancer.org/breast-cancer-staging/.
9. Foundation, N.B.C. *Treatment*. 2019 [cited 2020, March 5]; Available from: https://www.nationalbreastcancer.org/breast-cancer-treatment/.
10. Deshmukh, S.K., et al., *Emerging evidence for the role of differential tumor microenvironment in breast cancer racial disparity: a closer look at the surroundings.* 2017. **38**(8): p. 757-765.
11. Kim, H., et al., *The hypoxic tumor microenvironment in vivo selects the cancer stem cell fate of breast cancer cells.* 2018. **20**(1): p. 16.
12. Zamora-León, S.P., et al., *Expression of the fructose transporter GLUT5 in human breast cancer.* 1996. **93**(5): p. 1847-1852.
13. Warburg, O.J.S., *On the origin of cancer cells.* 1956. **123**(3191): p. 309-314.
14. Lin, H.H., et al., *Myeloid heme oxygenase-1 promotes metastatic tumor colonization in mice.* 2015. **106**(3): p. 299-306.
15. Orellana, R., et al., *Platelets enhance tissue factor protein and metastasis initiating cell markers, and act as chemoattractants increasing the migration of ovarian cancer cells.* 2015. **15**(1): p. 290.
16. Mehta, G., et al., *Opportunities and challenges for use of tumor spheroids as models to test drug delivery and efficacy.* 2012. **164**(2): p. 192-204.
17. Fennema, E., et al., *Spheroid culture as a tool for creating 3D complex tissues.* 2013. **31**(2): p. 108-115.
18. Hirschhaeuser, F., et al., *Multicellular tumor spheroids: an underestimated tool is catching up again.* 2010. **148**(1): p. 3-15.
19. Friedrich, J., et al., *Spheroid-based drug screen: considerations and practical approach.* 2009. **4**(3): p. 309.
20. LaBarbera, D.V., B.G. Reid, and B.H.J.E.o.o.d.d. Yoo, *The multicellular tumor spheroid model for high-throughput cancer drug discovery.* 2012. **7**(9): p. 819-830.
21. Kannan, S., et al., *Metabolism-Driven High-Throughput Cancer Identification with GLUT5-Specific Molecular Probes.* 2018. **8**(2): p. 39.

22. Fedie, J., et al. *Fructose uptake-based rapid detection of breast cancer*. in *2017 IEEE Life Sciences Conference (LSC)*. 2017. IEEE.
23. Chaudhuri, P.K., et al., *Topography induces differential sensitivity on cancer cell proliferation via Rho-ROCK-Myosin contractility.* Scientific Reports, 2016. **6**: p. 19672.
24. Begoyan, V.V., et al., *Multicolor GLUT5-permeable fluorescent probes for fructose transport analysis.* 2018. **54**(31): p. 3855-3858.
25. Hotaling, N.A., et al., *DiameterJ: A validated open source nanofiber diameter measurement tool.* Biomaterials, 2015. **61**: p. 327-338.
26. Schindelin, J., et al., *Fiji: an open-source platform for biological-image analysis.* 2012. **9**(7): p. 676-682.
27. Hodneland, E., et al., *CellSegm-a MATLAB toolbox for high-throughput 3D cell segmentation.* 2013. **8**(1): p. 16.
28. Mustafa, N.B.A., et al. *Image processing of an agriculture produce: Determination of size and ripeness of a banana*. in *2008 International Symposium on Information Technology*. 2008. IEEE.
29. Priya, V.L., K.J.I.J.O.E. Perumal, and C. Science, *Detecting the car number plate using segmentation.* 2014. **3**(10): p. 8823-8829.
30. Reneker, D.H., et al., *Bending instability of electrically charged liquid jets of polymer solutions in electrospinning.* 2000. **87**(9): p. 4531-4547.
31. Nurfaizey, A.H., et al., *Control of spatial deposition of electrospun fiber using electric field manipulation.* 2014. **9**(1): p. 155892501400900118.
32. Putti, M., et al., *Electrospinning poly (ε-caprolactone) under controlled environmental conditions: Influence on fiber morphology and orientation.* 2015. **63**: p. 189-195.
33. Hanumantharao, S.N., et al., *Engineered Three-Dimensional Scaffolds Modulating Fate of Breast Cancer Cells Using Stiffness and Morphology Related Cell Adhesion.* IEEE Open Journal of Engineering in Medicine and Biology, 2020. **1**: p. 41-48.
34. Dalton, P.D., et al., *Direct in vitro electrospinning with polymer melts.* 2006. **7**(3): p. 686-690.
35. Supaphol, P., C. Mit-Uppatham, and M.J.J.o.P.S.P.B.P.P. Nithitanakul, *Ultrafine electrospun polyamide-6 fibers: Effect of emitting electrode polarity on morphology and average fiber diameter.* 2005. **43**(24): p. 3699-3712.
36. Zhou, F.-L., R.-H. Gong, and I.J.J.o.M.S. Porat, *Three-jet electrospinning using a flat spinneret.* 2009. **44**(20): p. 5501-5508.
37. Subbiah, T., et al., *Electrospinning of nanofibers.* 2005. **96**(2): p. 557-569.
38. Bauer, A.L., T.L. Jackson, and Y.J.P.c.b. Jiang, *Topography of extracellular matrix mediates vascular morphogenesis and migration speeds in angiogenesis.* 2009. **5**(7).
39. Bauer, A.L., T.L. Jackson, and Y.J.B.j. Jiang, *A cell-based model exhibiting branching and anastomosis during tumor-induced angiogenesis.* 2007. **92**(9): p. 3105-3121.
40. Kovalenko, V., et al., *Interpretation of the IR spectrum and structure of cellulose nitrate.* 1994. **34**(4): p. 540-547.
41. Wang, X., et al., *Crystalline morphology of electrospun poly (ε-caprolactone)(PCL) nanofibers.* 2013. **52**(13): p. 4939-4949.
42. Varetti, E. and A.J.S.A.P.A.M.S. Müller, *Matrix isolation ir spectrum and force constants of CrO2Cl2.* 1978. **34**(9): p. 895-898.
43. Dübal, H.R. and M.J.T.J.o.c.p. Quack, *Tridiagonal Fermi resonance structure in the IR spectrum of the excited CH chromophore in CF3H.* 1984. **81**(9): p. 3779-3791.

44. Lazarev, Y.A., B. Grishkovsky, and T.J.B.O.R.o.B. Khromova, *Amide I band of IR spectrum and structure of collagen and related polypeptides.* 1985. **24**(8): p. 1449-1478.
45. Sigma, M. *IR Spectrum Table & Chart*. 2020 [cited 2020, March 5]; Available from: https://www.sigmaaldrich.com/technical-documents/articles/biology/ir-spectrum-table.html.
46. Ambasta, B., *Chemistry for engineers*. 2008: Laxmi Publications.
47. Ishida, T.J.B., *Low-barrier hydrogen bond hypothesis in the catalytic triad residue of serine proteases: correlation between structural rearrangement and chemical shifts in the acylation process.* 2006. **45**(17): p. 5413-5420.
48. Fesenko, O., L. Yatsenko, and M. Brodin. *Nanomaterials Imaging Techniques, Surface Studies, and Applications*. in *Springer Proceedings in Physics*. 2013. Springer.
49. Mathur, S., et al., *Chemical Vapor Growth of One-dimensional Magnetite Nanostructures.* 2008. **20**(8): p. 1550-1554.
50. Zussman, E., et al., *Tensile deformation of electrospun nylon-6, 6 nanofibers.* 2006. **44**(10): p. 1482-1489.
51. Arinstein, A., et al., *Effect of supramolecular structure on polymer nanofibre elasticity.* 2007. **2**(1): p. 59.
52. Lim, C., E. Tan, and S.J.A.P.L. Ng, *Effects of crystalline morphology on the tensile properties of electrospun polymer nanofibers.* 2008. **92**(14): p. 141908.
53. Mah, E.J., et al., *Collagen density modulates triple-negative breast cancer cell metabolism through adhesion-mediated contractility.* Scientific Reports, 2018. **8**(1): p. 17094.
54. Li, Q.S., et al., *AFM indentation study of breast cancer cells.* Biochemical and Biophysical Research Communications, 2008. **374**(4): p. 609-613.
55. Cavo, M., et al., *Microenvironment complexity and matrix stiffness regulate breast cancer cell activity in a 3D in vitro model.* Scientific Reports, 2016. **6**: p. 35367.
56. Dupont, S., et al., *Role of YAP/TAZ in mechanotransduction.* Nature, 2011. **474**(7350): p. 179-183.
57. Lin, F., et al., *Substrate Stiffness Coupling TGF-β1 Modulates Migration and Traction Force of MDA-MB-231 Human Breast Cancer Cells in Vitro.* ACS Biomaterials Science & Engineering, 2018. **4**(4): p. 1337-1345.
58. Wei, S.C., et al., *Matrix stiffness drives epithelial–mesenchymal transition and tumour metastasis through a TWIST1–G3BP2 mechanotransduction pathway.* Nature Cell Biology, 2015. **17**: p. 678.
59. Spill, F., et al., *Impact of the physical microenvironment on tumor progression and metastasis.* Current Opinion in Biotechnology, 2016. **40**: p. 41-48.
60. Liotta, L.A., J. Kleinerman, and G.M. Saldel, *The Significance of Hematogenous Tumor Cell Clumps in the Metastatic Process.* Cancer Research, 1976. **36**(3): p. 889.
61. Satoyoshi, R., et al., *Asporin activates coordinated invasion of scirrhous gastric cancer and cancer-associated fibroblasts.* Oncogene, 2015. **34**(5): p. 650-660.
62. Rubashkin, M.G., et al., *Force Engages Vinculin and Promotes Tumor Progression by Enhancing PI3K Activation of Phosphatidylinositol (3,4,5)-Triphosphate.* Cancer Research, 2014. **74**(17): p. 4597.
63. Jeon, H., et al., *Directing cell migration and organization via nanocrater-patterned cell-repellent interfaces.* Nature Materials, 2015. **14**: p. 918.